

## Terahertz Optics

Having learned how to generate and detect THz radiation, we are ready to discuss how to harness and manipulate THz waves. This chapter is devoted to materials, devices, and physical phenomena, which can be utilized in various THz applications.

### 5.1 Dielectric Properties of Solids in the Terahertz Region

THz optoelectronic devices bridge the technological gap inaccessible by RF and microwave techniques and infrared spectroscopy. The THz gap is also an intermediate spectral region for the optical properties of dielectrics. The Drude mechanism and Debye relaxation are dominant processes governing dielectric properties of solids in the low frequency region below the microwave band. These physical processes are probed by RF and microwave devices which measure the dielectric constants of materials. The low-frequency effects diminish in the THz region as frequency increases. On the higher frequency side, the mid-IR range, optical properties of dielectrics are overwhelmed by lattice vibrations, or more precisely, their IR-active quantized normal modes, optical phonons. Studying lattice vibrations is a major subject of infrared and Raman spectroscopy. The THz region is usually out of optical phonon resonances, but the low-energy tail of the spectrum is a major source of absorption in this spectral range. The dielectric response of vibrational modes decays as frequency decreases in the THz region.

The Drude mechanism accounts for the transport properties of free carriers in a material. The electrical conductivity derived from the Drude model is expressed as

$$\sigma(\omega) = \frac{\sigma_0}{1 - i\omega\tau} \quad (5.1)$$

with the static conductivity

$$\sigma_0 = \frac{n_q q^2 \tau}{m_q}, \quad (5.2)$$

where  $n_q$  is the charge density,  $m_q$  is the particle mass, and  $\tau$  is the relaxation time. Thus, the electric permittivity of the material is given as

$$\epsilon(\omega) = \epsilon_0 + i \frac{\sigma(\omega)}{\omega} = \epsilon_0 + \frac{i\sigma_0}{\omega(1 - i\omega\tau)}. \quad (5.3)$$

From this equation we can see that the relaxation time is the sole parameter governing the frequency-dependent optical properties. The relaxation time of a high-quality intrinsic semiconductor is in the vicinity of a picosecond at room temperature. The time scale is a few orders of magnitude shorter in most dielectric media. It is noteworthy that the inverse of the time scale falls into the THz range.

Dielectric relaxation, also called Debye relaxation, refers to the delayed response of a dielectric medium to applied electric fields. The momentary delay of the response is accounted for by random thermal fluctuations which slow down the reorientations of the dipole moments in the material. The simplest model to describe the relaxation process is expressed as the Debye equation

$$\epsilon(\omega) = \epsilon(\infty) + \frac{\epsilon(0) - \epsilon(\infty)}{1 - i\omega\tau_D}, \quad (5.4)$$

where the frequency-dependent electric permittivity is determined by the static permittivity  $\epsilon(0)$ , the high-frequency permittivity  $\epsilon(\infty)$ , and the Debye relaxation time  $\tau_D$ . The Debye relaxation time varies widely depending on the material system. Typical time scales range from microseconds to nanoseconds at room temperature.

Usually the lowest optical phonon resonance of a dielectric crystal is in the vicinity of 10 THz. A simple approximation of the dielectric response of lattice vibrations is the harmonic oscillator model described in section 2.1.4. The electric permittivity derived from the model is expressed as

$$\epsilon(\omega) = \epsilon_L(0) + \frac{f_L}{\omega_L^2 - \omega^2 - i\omega\gamma_L}, \quad (5.5)$$

where  $\epsilon_L(0)$  is the static permittivity of lattice vibrations,  $\omega_L$  is the resonance frequency,  $f_L$  is the oscillator strength, and  $\gamma_L$  is the damping constant.

These three microscopic processes, the Drude mechanism, dielectric relaxation, and lattice vibrations, are dominant absorption processes of solids in the THz region. Figure 5.1 depicts the typical dielectric response at THz frequencies. The effects of the three absorption mechanisms are shown in the form of the refractive index

$$n(\omega) = \Re[\sqrt{\epsilon_r(\omega)}] \quad (5.6)$$

and the absorption coefficient

$$\alpha(\omega) = \frac{2\omega}{c} \Im[\sqrt{\epsilon_r(\omega)}] \quad (5.7)$$

in a log scale as functions of frequency.

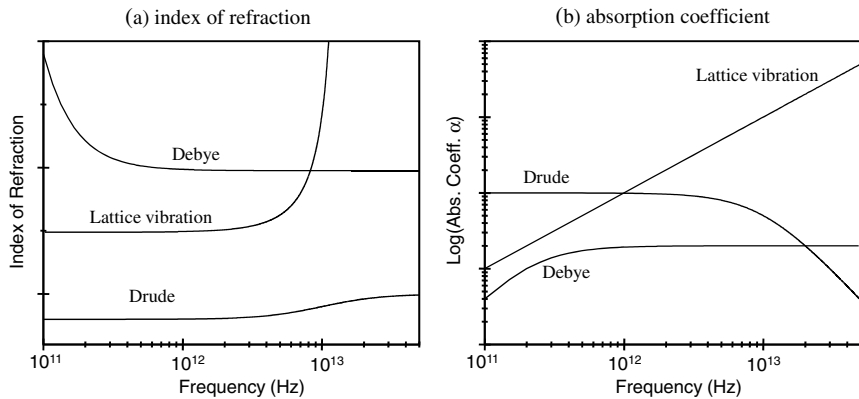


**Fig. 5.1.** Frequency-dependent refractive index and absorption coefficient of a typical dielectric medium in the THz region

## 5.2 Materials for Terahertz Optics

The characteristic optical properties of solids in the THz region depend on different physical mechanisms from those in other spectral ranges. Free-carrier effects, in particular, are relatively strong; phonon resonances make materials opaque in this spectral range. Ordinary glasses commonly used in optical regions are useless for THz applications because extrinsic dielectric losses from charged defects are too high. Some material types, however, are highly transparent at THz frequencies. Transmissive THz materials include polymers, dielectrics, and semiconductors. Polymers such as polyethylene, Teflon (PTFE), and TPX are transparent and almost dispersionless at THz frequencies. Their absorption coefficients are less than 0.5 cm<sup>-1</sup> at 1 THz, and show nearly quadratic increases with frequency. The average refractive indices vary little among the polymers ranging from 1.4 to 1.5. Commonly used dielectrics and semiconductors are silicon, germanium, gallium arsenide, quartz, fused silica, and sapphire. Silicon is the most transparent and the least dispersive material among the dielectrics as well as the polymers. The absorption coefficient of a high-purity crystal is less than 0.1 cm<sup>-1</sup> below 3 THz, and the variation of the refractive index, 3.4175, is less than 0.0001 in the same range. The effects of free carriers and lattice vibrations in other dielectrics and semiconductors are far greater than those in silicon. Basic optical components such as windows

and lenses are made of transmissive THz materials. Polished metal surfaces or metal coating mirrors are commonly used as THz reflectors. Typical reflectivity is 98-99% in the THz region.

### 5.2.1 Polymers

The polyethylene family, including high-density polyethylene (HDPE) and low-density polyethylene (LDPE), is the most widely used polymer group because of its excellent clarity. HDPE and LDPE also have other favorable properties: they are isotropic, easily machinable, and chemically stable. High-quality polyethylene has a sharp lattice mode at 2.2 THz with a bandwidth of 0.2 THz. Although this shows its high degree of ordered structure, the absorption line is problematic for applications near that frequency. The refractive index of HDPE, 1.526, is slightly larger than that of LDPE, 1.513. PTFE is highly transparent on the lower frequency side of the spectrum, yet its absorption is a little higher than that of polyethylene. It becomes significantly lossy above 3 THz. The refractive index is 1.432 below 3 THz. Its high resistance to corrosion and adsorption makes this material suitable for chemical and biological studies. Polypropylene (PP) is another transmissive material, though it is not as widely used as other polymers. Its absorption spectrum is similar to that of PTFE below 3 THz. It has multiple lattice modes above that frequency. The average refractive index is 1.498 on the low frequency side. TPX, polyolefine based on poly 4 methyl pentene-1, is transparent not only at THz frequencies, but also in the visible spectral range. Its THz refractive index, 1.457, is also close to its optical counterpart. This distinctive advantage has been exploited in many quasi-optical systems. In the THz region its absorption coefficient is slightly higher than that of polyethylene, but

**Table 5.1.** Optical Constants of Polymers

Polymer	$n$	$\alpha$ ( $\text{cm}^{-1}$ ) at 1 THz
LDPE <sup>a,c</sup>	1.51	0.2
HDPE <sup>a,c,f,g</sup>	1.53	0.3
PTFE <sup>a,d,g</sup>	1.43	0.6
PP <sup>a,d,g</sup>	1.50	0.6
TPX <sup>a,b</sup>	1.46	0.4
Tsurupica <sup>h</sup>	1.52	0.4

<sup>a</sup>reference [113]

<sup>b</sup>reference [114]

<sup>c</sup>reference [115]

<sup>e</sup>reference [116]

<sup>f</sup>reference [117]

<sup>g</sup>reference [118]

<sup>h</sup><http://www.mtinstruments.com/thzlenses/index.htm>

lower than that of PTFE. It is more mechanically rigid than other polymers. Tsurupica, formerly known as picarin, is a relatively new material developed at RIKEN in Japan. Tsurupica is also highly transparent in both the THz and visible spectral ranges. The THz refractive index is 1.52, which is almost the same as for visible light. Mechanically, it is strong enough to withstand optical polishing.

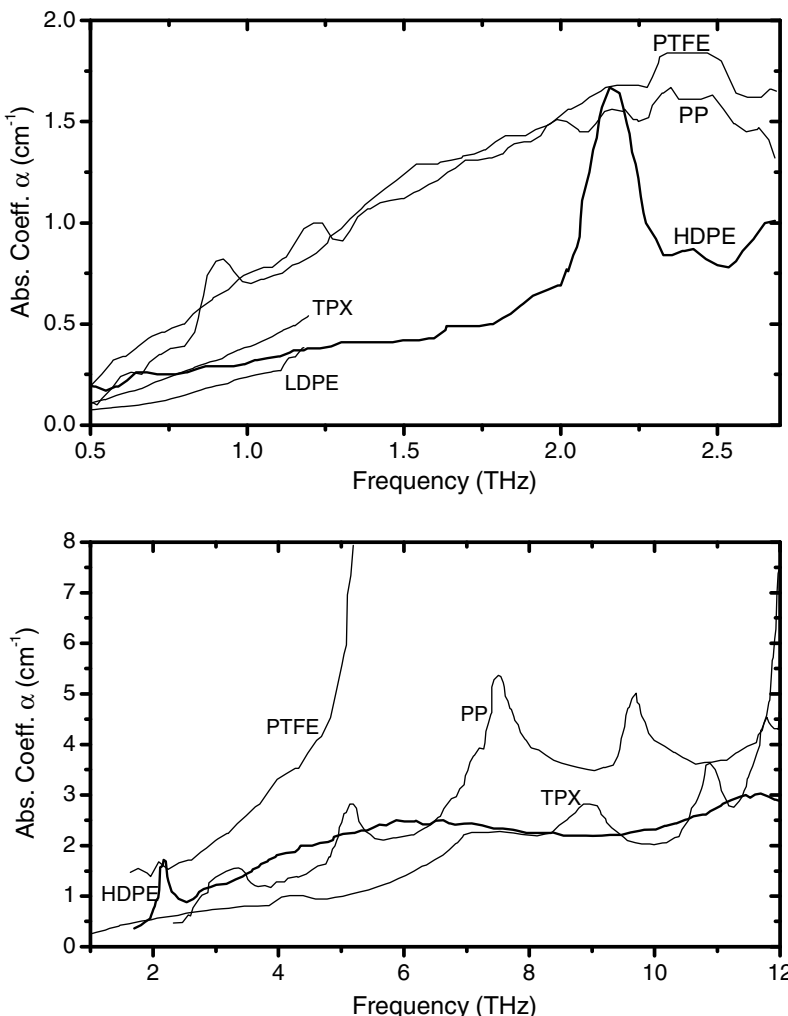


**Fig. 5.2.** Absorption coefficients of the polymers versus frequency in the two spectral ranges of (a) 0.5–2.5 THz and (b) 2–12 THz. (Data from Refs. [113, 114, 115, 116, 117, 118])

The average THz refractive indices over the range 0.5-3 THz and the absorption coefficients at 1 THz are given in Table 5.1 for the aforementioned polymers. The details of the frequency-dependent absorption are shown in Fig. 5.2 for two spectral windows, (a) the low frequency side, 0.5-2.5 THz, and (b) the high frequency side, 2-12 THz.

### 5.2.2 Dielectrics and Semiconductors

Crystalline silicon, whose optical properties in the THz region haven been studied more extensively than any other material, is not only the most transparent but also the least dispersive medium in that spectral range. Moreover, its mechanical and electrical properties are known in great detail, its price is low, high-quality crystals are readily available, and there are numerous fabrication techniques specified for the material. Silicon is arguably the most important raw material for THz device development.

Crystals of high symmetry are inactive in the infrared region because first-order transitions between lattice vibration modes are forbidden by symmetric selection rules. The lack of first-order absorption in silicon can be simply understood by the symmetric charge distribution in the crystal structure. Crystalline silicon, composed of one element, has no dipole moment to be coupled with external electric fields. Thus, absorption involving lattice vibrations

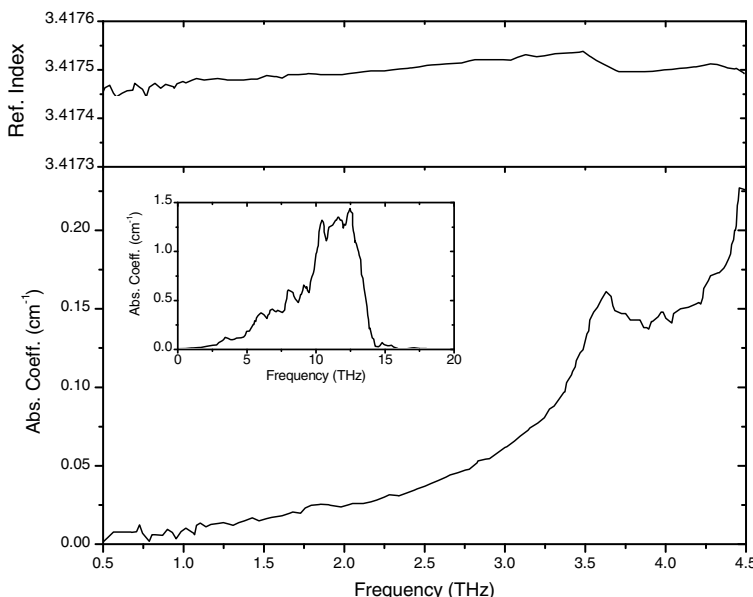


**Fig. 5.3.** Dispersion and absorption spectra of float-zone, high-resistivity silicon. Calculated two-phonon absorption in the infrared region is shown in inset. (Data from Refs. [119, 120])

should be dominated by second-order (two-phonon) processes. Its two-phonon absorption coefficient is estimated to be less than  $0.1 \text{ cm}^{-1}$  below 3 THz [120]. On the low frequency side, the experimental data on absorption of commonly used silicon wafers cannot be explained by two-phonon contributions alone. The main culprit causing the additional absorption is free carriers from defect sites. Measurements on high-resistivity silicon samples show that absorption is proportional to conductivity, which is linearly dependent on carrier concentration, in the spectral range where two-phonon absorption is negligible.

High-purity silicon, produced using the float-zone crystal growth method, has a remarkably low carrier concentration ( $< 4 \times 10^{11} \text{ cm}^{-3}$  for n-type) and high resistivity ( $> 10 \text{ k}\Omega\text{-cm}$ ). Figure 5.3 shows the refractive index and the absorption spectrum of float-zone, high-resistivity silicon in the spectral range 0.5-4.5 THz [119]. The spectral feature, including the peak near 3.6 THz, is consistent with the calculated two-phonon absorption shown in inset [120].

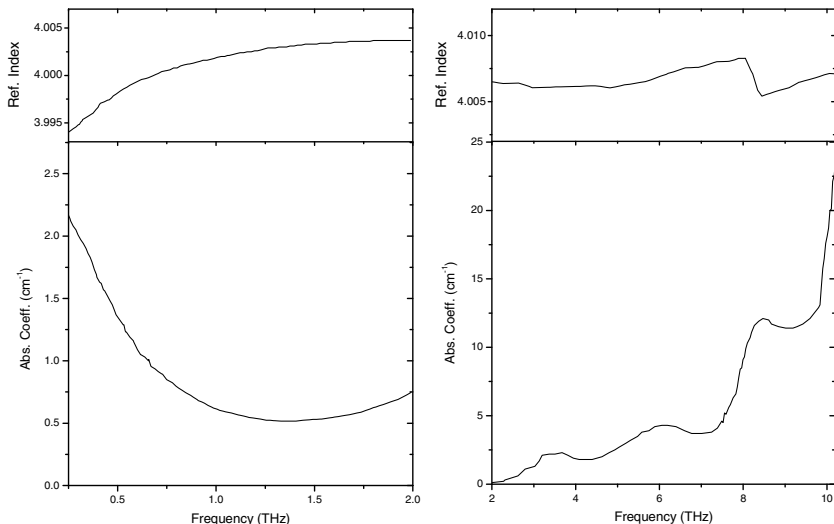


**Fig. 5.4.** Dispersion and absorption spectra of intrinsic germanium in the spectral ranges 0.2-2 THz and 2-10 THz. (Data from Refs. [23, 121].

As germanium has the same crystal structure as silicon, no first-order absorption is allowed. A reasonable yet casual guesswork may speculate that crystalline germanium should have similar optical properties as silicon in the THz region. A closer look, however, defies this prediction. Intrinsic germanium has a relatively small bandgap energy (0.66 eV). Consequently, the intrinsic carrier concentration at room temperature,  $2 \times 10^{13}$ , is significantly higher than that of silicon, and the resistivity,  $46 \Omega\text{-cm}$ , is relatively low. The carrier concentration is high enough that the Drude mechanism dominates the absorption of germanium in the THz region: the relaxation times for the elec-

trons and the holes are 0.6 and 0.7 THz, respectively. The left panel of Fig. 5.4 shows the dispersion and absorption spectra of an intrinsic germanium crystal [23]. The spectral features are consistent with the Drude model discussed in section 5.1. The optical constants in the spectral range 2-10 THz are shown in the right panel of Fig. 5.4 [121]. Multi-phonon resonances are discernible at 3.5, 6.0, and 8.5 THz. The Drude mechanism is negligible in this spectral region.

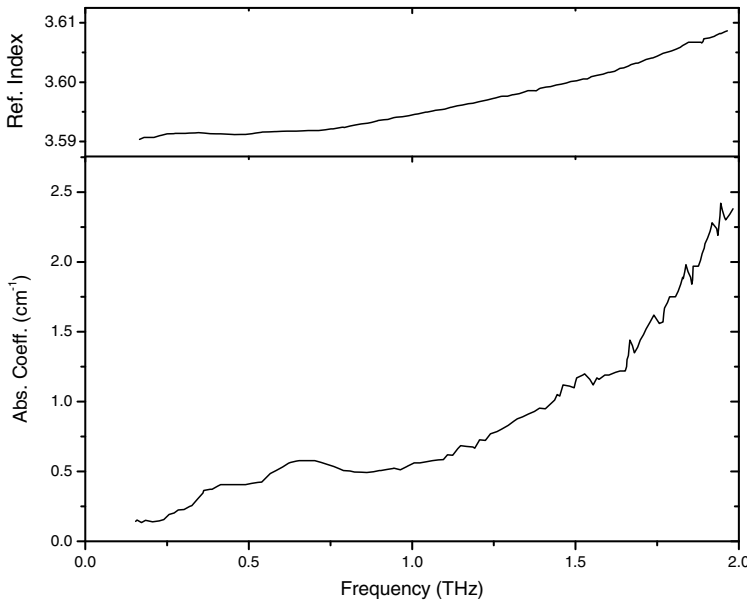


**Fig. 5.5.** Dispersion and absorption spectra of crystalline GaAs. (Data from Ref. [23])

The refractive index and absorption spectrum of gallium arsenide (GaAs) are shown in Fig. 5.5 [23]. The highly refined growth techniques of crystalline GaAs routinely produce high-resistivity ( $>10 \text{ M}\Omega\text{-cm}$ ) crystals with very low carrier concentrations. The primary THz absorption mechanism in GaAs involves the optical phonon mode at 8.1 THz which has a large density of states due to the flat band structure. First-order absorption is allowed in the III-V material because the charge distribution between the two elements of the crystal is asymmetric, and the consequent dipole moments are directly coupled with an applied electric field. The phonon resonance is strong enough to give rise to the gradual increase of absorption as shown in Fig. 5.5, even though the spectral range is far from the resonant frequency. The two small peaks featured at 0.4 and 0.7 THz are accounted for by a two-phonon process in which an optical phonon is created and a LA phonon is annihilated [122].

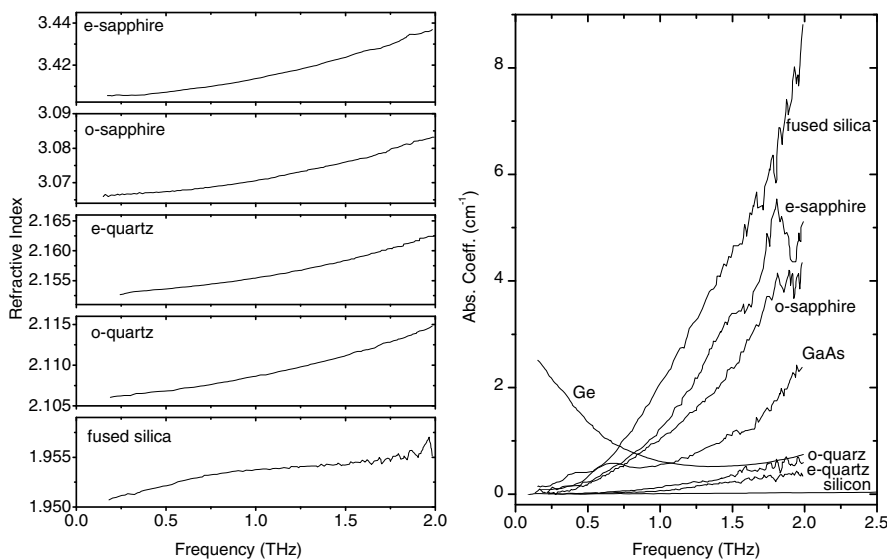


**Fig. 5.6.** Dispersion and absorption spectra of sapphire, quartz, and fused silica in the spectral range 0.2-2 THz. (Data from Ref. [23])

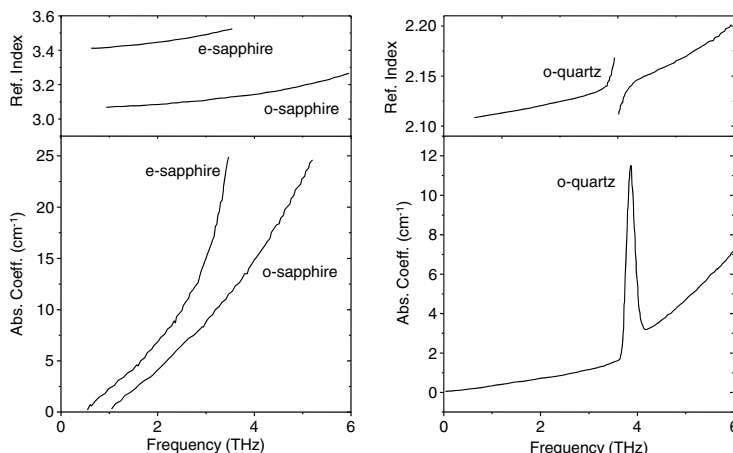


**Fig. 5.7.** Dispersion and absorption spectra of sapphire and quartz in the spectral range 1-6 THz. (Data from Ref. [121])

Absorption of crystalline sapphire, crystalline quartz, and fused silica is substantially higher than that of silicon in the THz region, but their high transmittance in the visible range is a useful property for some applications. The dispersion and absorption spectra for the dielectrics in the spectral range 0.2-2 THz are shown in Fig. 5.6. Sapphire and quartz are birefringent, thus

their optical constants have different values for ordinary and extraordinary rays. The lack of long-range order in fused silica facilitates the coupling of THz fields with multi-mode lattice vibrations, which gives rise to the substantially stronger absorption compared with that of crystalline quartz, while its refractive index is slightly smaller. Figure 5.7 shows the optical constants of sapphire and quartz in the spectral range 1-6 THz [121]. A strong ordinary ray absorption line is featured at 3.87 THz.

### 5.2.3 Conductors

The reflectivity of a metal surface is near unity in the THz region, and hence metal-coated mirrors are widely used as reflectors for THz applications. Common metals such as copper, silver, gold, and aluminium are adequate for this purpose. The optical properties of a metal surface at THz frequencies are well accounted for by the Drude model. Moreover, the Drude conductivity is further simplified as

$$\sigma(\omega) = \frac{\sigma_0}{1 - i\omega\tau} \cong \sigma_0, \quad (5.8)$$

because  $\omega\tau \ll 1$ , where the relaxation times of these common metals are on the order of  $10^{-14}$  s. The electrical conductivities of common metals are given in Table 5.2. The penetration depth,  $\delta = \sqrt{2/\omega\mu_0\sigma_0}$ , is less than 100 nm at 1 THz for common metals, thus a few-micron-thick layer is sufficient for a reflector.

**Table 5.2.** Electrical Conductivity and Penetration Depth

	Cu	Ag	Au	Al
$\sigma_0$ ( $10^6$ S·m $^{-1}$ )	59.6	63.0	45.2	37.8
$\delta$ at 1 THz (nm)	65.2	63.4	74.9	81.9

When an electromagnetic wave bounces off the interface of air and metal, the reflectivity at normal incidence has the form

$$R(\omega) = \left| \frac{\sqrt{\epsilon_r(\omega)} - 1}{\sqrt{\epsilon_r(\omega)} + 1} \right|^2, \quad (5.9)$$

where the complex dielectric constant is expressed as

$$\epsilon_r(\omega) = \epsilon_b + i \frac{\sigma(\omega)}{\epsilon_0\omega} \cong i \frac{\sigma_0}{\epsilon_0\omega}, \quad (5.10)$$

where  $\epsilon_b$  is the contribution from bound electrons. Since  $\sigma_0/\epsilon_0\omega \gg \epsilon_b$  in the THz region, the equation for the reflectivity is reduced to

$$R(\omega) \cong 1 - \sqrt{\frac{8\epsilon_0\omega}{\sigma_0}}. \quad (5.11)$$

Figure 5.8 shows the reflectance spectra of silver, copper, gold, and aluminium at normal incidence. The solid lines depict calculations using Eq. 5.11, which agree well with the experimental data of references [123] and [124].

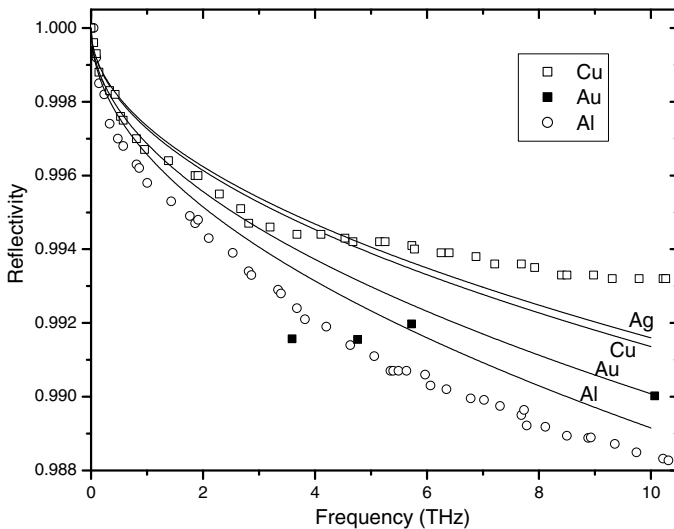


**Fig. 5.8.** Reflectivity versus frequency for Cu, Ag, Au, and Al. Solid lines indicate calculations using Eq. 5.11. Solid squares, open squares, and open circles are experimental data for gold, copper, and aluminium, respectively. (Data from Refs. [123, 124])

So far, we have neglected the real part of  $\epsilon_r$  because it is negligible, compared with the imaginary part. It is negative and independent of frequency in the THz region. Its absolute value is much greater than unity. Including the real part, we can approximate Eq. 5.10 as

$$\epsilon_r(\omega) \cong -\frac{\sigma_0\tau}{\epsilon_0} + i\frac{\sigma_0}{\epsilon_0\omega}. \quad (5.12)$$

Given that  $\tau=7.5$  and 25 fs for Al and Cu [124], we obtain

$$\text{Al : } \epsilon_r(\nu) = -3.2 \times 10^4 + i 6.7 \times 10^5 \nu^{-1} \quad (5.13)$$

$$\text{Cu : } \epsilon_r(\nu) = -1.7 \times 10^5 + i 1.1 \times 10^6 \nu^{-1} \quad (5.14)$$

where  $\nu = \omega/2\pi$  in THz.

An interesting material system for THz applications is transparent conductors such as tin doped indium oxide (ITO). Optical transmittance of ITO

is reported as high as 95% while the conductivity reaches up to  $10^6 \text{ S}\cdot\text{m}^{-1}$ . A conductivity of  $10^6 \text{ S}\cdot\text{m}^{-1}$  corresponds to 98% reflectivity at 1 THz and 500 nm penetration depth. This unique property provides a special use for THz applications. A thin layer of ITO coated on a glass substrate can be utilized as a dichroic mirror reflecting THz radiation while transmitting an optical beam.

## 5.3 Optical Components

### 5.3.1 Focusing Elements

Off-axis parabolic mirrors are broadly used to focus or collimate THz beams. The reflective surface of an off-axis parabolic mirror, formed when a partial section is cut out from a paraboloid, as shown in Fig. 5.9(a), is usually coated with common metals such as aluminium and gold, whose reflectivity is in the vicinity of 99 % in the THz region (see Fig. 5.8). A clear advantage of reflective optics over conventional lenses is that there is little loss by reflection and absorption. It also works over a broad spectral range, including the optical region, without spectral aberration. Furthermore, parabolic mirrors are free from spherical aberration, focusing a parallel beam to a point or forcing the radiation from a point source highly collimated. This is an important trait, especially for a quasi-optical THz system dealing with diffraction-limited beams. Because the alignment of an off-axis parabolic mirror is highly sensitive to astigmatism and other collimation errors, a high-precision procedure is necessary in practical applications to avoid them.

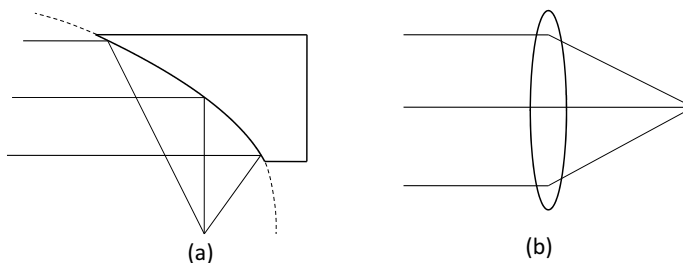


**Fig. 5.9.** (a) Off-axis parabolic mirror and (b) singlet lens

As discussed in section 3.2.3, substrate lenses, collimating lenses and hyper-hemispherical Lenses, are being used for collecting radiation from photoconductive emitters and coupling it to receivers. The low-loss polymers, dielectrics, and semiconductors (see section 5.2) potentially make good materials for THz lenses. THz singlet lenses for general purposes made of silicon, polyethylene, teflon, and Tsurupica, are commercially available.

Diffractive optics, such as Fresnel zone-plates, have also been fabricated and tested [125, 126], but are not broadly available at present.

### 5.3.2 Antireflection Coatings

Fresnel, or reflection, loss is one of the main loss mechanisms in THz optical systems, because the majority of low-loss dielectrics and semiconductors used for THz components have relatively large refractive indices in the THz region. Antireflection (AR) coatings can greatly reduce Fresnel losses.

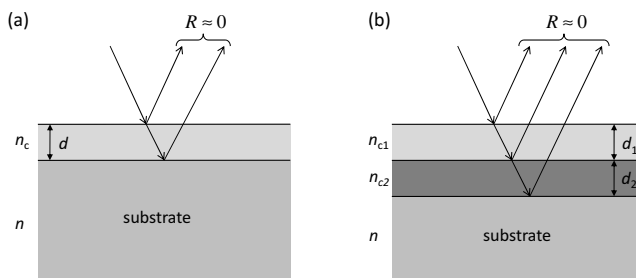


**Fig. 5.10.** Schematic diagrams for (a) a single-layer and (b) multilayer antireflection coatings.

Figure 5.10 illustrates a schematic representation of single-layer and multilayer AR coatings. The AR coating schemes exploit the destructive interference between the reflective waves from multiple interfaces. Single-layer AR coatings require two conditions. First, the reflection coefficients of the two interfaces at normal incidence must be equal,

$$\frac{1 - n_c}{1 + n_c} = \frac{n_c - n}{n_c + n}, \quad (5.15)$$

which yields

$$n_c = \sqrt{n}. \quad (5.16)$$

Second, in order for the two reflected waves to destructively interfere the effective path length in the coating layer must be a half wavelength of the incoming wave, i.e., the coating layer thickness is

$$d = \frac{\lambda}{4n_c}. \quad (5.17)$$

A small number of THz-AR coating techniques have been developed so far. Polyethylene ( $n \approx 1.5$ ) AR coatings on quartz, sapphire, and CaF<sub>2</sub> have been constructed by a thermal bonding technique in which a polyethylene film is placed in physical contact with a substrate and heated to a temperature just

below its melting point [127]. Another promising coating material is silicon oxide ( $\text{SiO}_2$ ), whose refractive index ( $n = 2$ ) is close to the square root of Ge ( $n = 4.0$ ) and GaAs ( $n = 3.6$ ) refractive indices. An AR coating technique used with this material is to glue a  $\text{SiO}_2$  plate onto Ge and GaAs wafers and control the coating thickness by mechanical polishing [128]. Epitaxial growth techniques control film thicknesses with high accuracy, but a technical impediment for growing THz AR coatings is that the required film thickness, in the range of 10-100  $\mu\text{m}$ , exceeds the capabilities of typical epitaxial techniques. This technical difficulty was circumvented when a plasma-enhanced chemical-vapor deposition (CVD) method made a huge improvement on the film growth speed. It has been used to grow  $\text{SiO}_x$  AR coatings on Ge wafers [129]. A drawback of these single-layer AR coatings is that the AR bandwidth is narrow. A broadband AR bandwidth can be obtained by using a multilayer interference film. The plasma-enhanced CVD technique has been applied to grow multilayer AR coatings on Ge substrates [130].

### 5.3.3 Bandpass Filters

Thin metallic meshes have been used as bandpass filters in the THz region. The optical properties of mesh filters are accounted for by the dynamics of surface plasmon polaritons in metal-dielectric interfaces. We will review this subject from a broader perspective in section 5.5.3. In the present section, we will approach this problem from a phenomenological point of view. A typical structure of mesh filters is the inductive grid shown in Fig. 5.11(a). An electromagnetic wave incident on the metal grid structure gives rise to electromagnetic induction as the field induced surface currents flow in the closed loops of the grid. At the same time, charge distribution varies in time depending on the field amplitude, phase, and polarization. Elaborating on this picture systematically, we can obtain an equivalent circuit representation based on the transmission line theory as a simple model to describe the optical properties of the metal grid [131]. The inset of Fig. 5.11(b) shows an equivalent circuit to the inductive grid. The transmission of this circuit is expressed as

$$T(\omega) = \frac{(\omega^2 - \omega_0^2)^2 R^2 + \omega^2 \omega_0^2 Z_0^2}{(\omega^2 - \omega_0^2)^2 (1 + R^2) + \omega^2 \omega_0^2 Z_0^2} \quad (5.18)$$

$$\approx \frac{\omega^2 \omega_0^2 Z_0^2}{(\omega^2 - \omega_0^2)^2 + \omega^2 \omega_0^2 Z_0^2} \quad \text{for } R \ll Z_0, \quad (5.19)$$

where  $\omega_0$  is the resonant frequency,  $R$  is the loss resistance, and

$$Z_0 = \omega_0 L = \frac{1}{\omega_0 C} \quad (5.20)$$

is the normalized impedance of  $L$  and  $C$  at resonance. Fig. 5.11(b) shows the transmission spectrum for  $R \ll Z_0$ . The resonant wavelength  $\lambda_0 = 2\pi c/\omega_0$  is on the same scale as the grid period  $g$ .

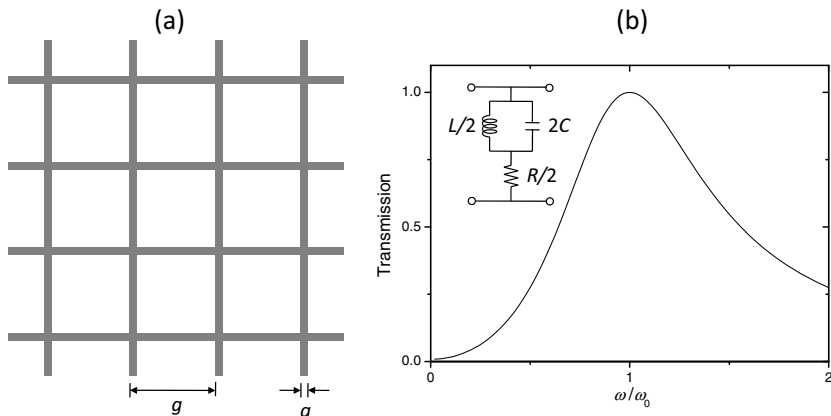


**Fig. 5.11.** Metal-mesh filter: (a) inductive grid structure and (b) transmission spectrum. Inset shows the equivalent circuit.

Several different types of grid structures have been examined in an effort to better control the transmission band structure. The array of cross-shaped apertures shown in Fig 5.12(a) [132] is one of them which has some useful properties. The transmission spectra of four filters with different dimensions ( $g/a/b$  in  $\mu\text{m}$  are 402/251/66, 201/126/33, 154/98/28, and 113/71/19) are shown in Fig 5.12(b). The peak transmissions at the central frequencies are almost unity for all of the filters. The central frequency of the passband is mainly determined by the length of the cross  $a$ . The bandwidth tends to get narrower as the ratios of  $g/a$  and  $g/b$  are increased.

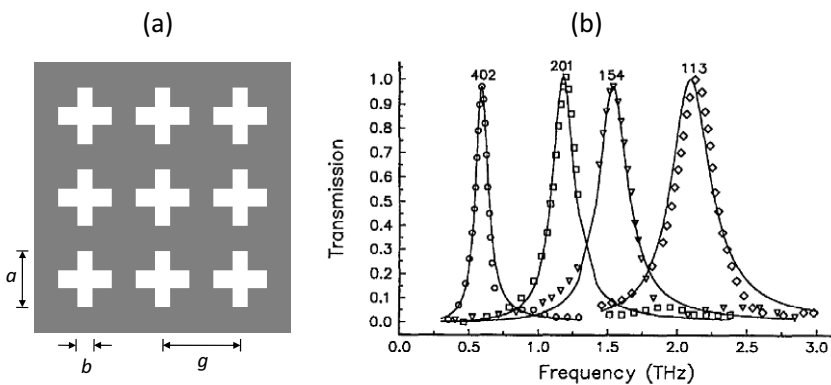


**Fig. 5.12.** Resonant bandpass filter with an array of cross-shaped apertures: (a) schematic diagram of the structure and (b) transmission spectra for the four filters whose dimensions  $g/a/b$  in  $\mu\text{m}$  are 402/251/66, 201/126/33, 154/98/28, and 113/71/19. (Reprinted from [132].)

### 5.3.4 Polarizers

Free-standing metal wire grids are commonly used as polarizers in the THz region. Figure 5.13 illustrates the structure of a typical wire-grid polarizer with a circular frame: the thin metal wires, each with diameter  $a$ , form the regular array of the grid with period  $g$ , placed in a flat plane. The underlying mechanism of its polarization selectivity is quite simple. Imagine an electromagnetic wave is incident on a wire-grid polarizer. If the electric field is parallel to the wires, the electrons in the wires can move freely along the wire direction responding to the incident field. In this case, the polarizer behaves much like a typical metal surface, thus most of the incident beam is reflected by the polarizer. On the other hand, if the field is perpendicular to the wires, the wave does not see much of the wires and passes through the polarizer, because the movements of the electrons in the direction perpendicular to the wires are highly restricted. In general, the transmission at an angle  $\theta$  between the grid direction and the polarization has the following relation:  $T(\theta) = \sin^2 \theta$ .

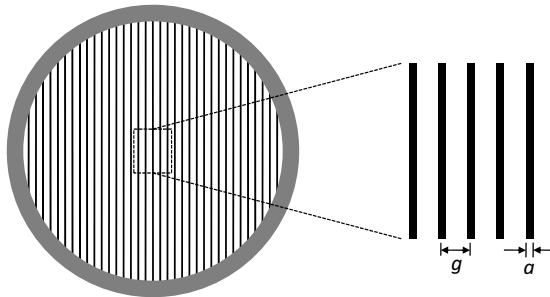


**Fig. 5.13.** Wire-grid polarizer. Transmission and extinction ratio are determined by the grid period  $g$  and the wire diameter  $a$ .

Wire grids are usually made of tungsten because it has the highest tensile strength among metals and excellent corrosion resistance. The wire diameter is  $\sim 10 \mu\text{m}$ , and the grid period is in the range of  $20\text{-}200 \mu\text{m}$ . In practical applications, the transmission does not disappear completely when the field is parallel to the grid direction. The distinction ratio  $T_{\perp}/T_{\parallel}$  is enhanced as the grid period  $g$  is decreased, while the cutoff frequency of  $T_{\perp}$  is reduced at the same time. For a polarizer with  $a=10 \mu\text{m}$  and  $g=25 \mu\text{m}$ , it is measured that  $T_{\perp}$  is about 0.98 at 1 THz and drops to 0.95 at 3 THz, and  $T_{\perp}/T_{\parallel}$  is  $\sim 1000$  at 1 THz and  $\sim 200$  at 3 THz. The reflectivity of a grid polarizer is usually higher than 0.95 in a broad spectral range for a field parallel to the grid direction, thus wire-grid polarizers are often used as beam splitters.

### 5.3.5 Wave Plates

A wave plate is an optical component used to control the polarization state of light. A birefringent crystal has different refractive indices for different polarizations: ordinary and extraordinary refractive indices  $n_o$  and  $n_e$ . Using the birefringence of crystals, we can modify the waves polarization state. For two monochromatic waves with their polarizations parallel to the ordinary and extraordinary axes, propagating a distance  $d$  in a birefringent crystal, the phase delay  $\Delta\phi$  between them is given as

$$\Delta\phi = \frac{\omega}{c}(n_e - n_o)d. \quad (5.21)$$

The thickness of a half-wave plate is chosen to produce a  $\pi$  phase delay so that the polarization of linearly polarized light can be rotated from 0 to  $90^\circ$  by adjusting the relative angle between the optic axis and the incident polarization. The  $\pi/2$  phase delay of a quarter-wave plate changes linearly polarized light to a circularly polarized light and vice versa when the linear polarization is aligned to dissect the ordinary and extraordinary axes. In between, any arbitrary elliptical polarization state can be obtained.

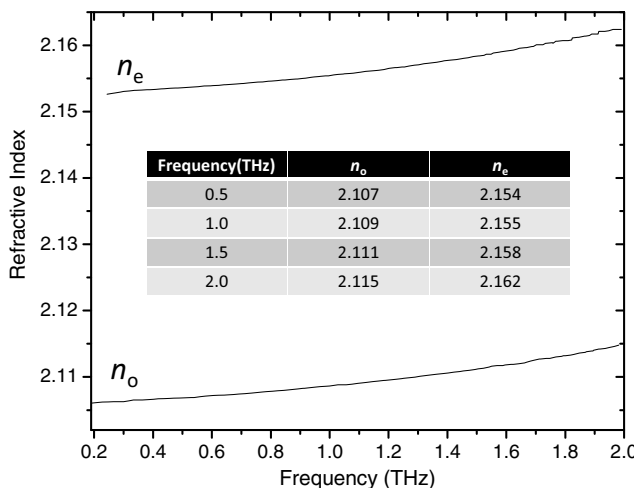


**Fig. 5.14.** Ordinary and extraordinary refractive indices of crystalline quartz in the THz region. (Data from Ref. [23])

Crystalline quartz is a birefringent crystal with some excellent properties for use as a wave plate. As shown in Figs. 5.6 and 5.7, quartz is strongly birefringent as well as highly transparent in the THz region. Figure 5.14 shows the ordinary and extraordinary refractive indices of quartz in the THz region. For  $\Delta n = n_e - n_o \simeq 0.047$  in this spectral range, the thickness of a quarter wave plate is determined to be

$$d_{\frac{\lambda}{4}} = \frac{c}{4\nu\Delta n} \simeq \frac{1.6}{\nu(\text{in THz})} \quad (\text{in mm}), \quad (5.22)$$

where  $\nu = \omega/2\pi$  is the frequency.

A significant drawback of a conventional birefringent wave plate is that it can only be used at a single wavelength. One approach to broaden the bandwidth is to fabricate a wave plate by stacking up multiple quartz plates. The THz achromatic quarter-wave plate made of six quartz plates has an almost flat phase retardation from 0.3 to 1.7 THz [133]. Another technique is to electrically control the birefringence of liquid crystal. With this technique, the phase delay at 1 THz is continuously tunable from 0 to  $\pi/2$  by adjusting the bias voltage [134].

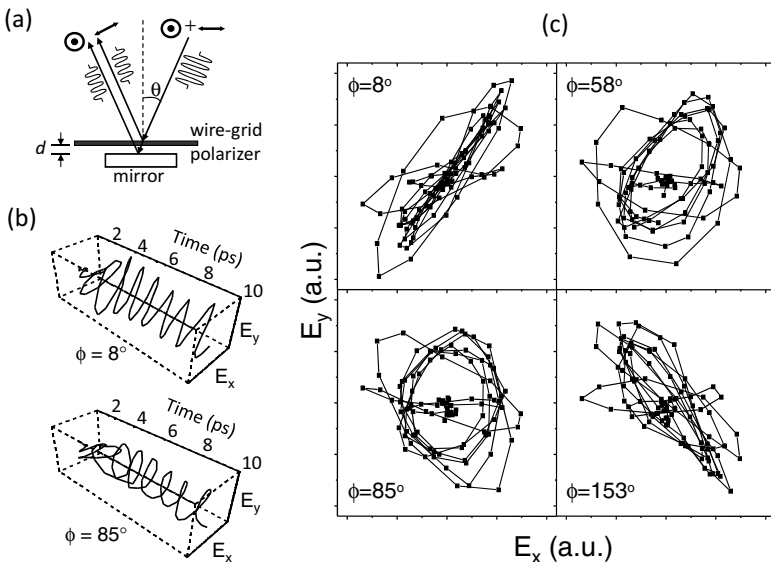


**Fig. 5.15.** (a) Schematic diagram of the broadband THz wave plate consisting of a wire-grid polarizer and a mirror. (b) Three-dimensional plots of THz E-field vectors for  $\Delta\phi = 8^\circ$  and  $85^\circ$ . (c) Polarization trajectories in the x-y plane for  $\Delta\phi = 8^\circ$ ,  $58^\circ$ ,  $85^\circ$ , and  $153^\circ$ . (Data from Ref. [135])

An alternative method to control THz polarization is illustrated in Fig. 5.15(a) [135]. Elliptical polarization can be obtained from the reflection of a linearly polarized THz wave by a combination of a wire-grid polarizer and a mirror with variable spacing  $d$ . The mirror and the polarizer reflect two perpendicularly polarized THz waves, and the phase delay

$$\Delta\phi = \frac{\omega}{c} \frac{2d}{\cos\theta}, \quad (5.23)$$

where  $\theta$  is the incident angle, is controlled by adjusting the spacing  $d$ . Figure 5.15(b) shows the THz E-field vectors of the linearly ( $\Delta\phi = 8^\circ$ ) and circularly ( $\Delta\phi = 85^\circ$ ) polarized THz pulses in the x-y plane. The phase delay is continuously tunable, and several snap shots of the phase control are shown in Fig. 5.15(c): the polarization trajectories in the x-y plane for  $\Delta\phi = 8^\circ$ ,  $58^\circ$ ,  $85^\circ$ , and  $153^\circ$ .

## 5.4 Terahertz Waveguides

A waveguide is a device used to carry electromagnetic waves from one place to another without significant loss in intensity while confining them near the propagation axis. The most common type of waveguides for radio waves and microwaves is a hollow metal pipe. Waves propagate through the waveguide, being confined to the interior of the pipe. A representative waveguide in the optical region is an optical fiber. Fiber-optic communication and a variety of other applications exploit the extremely low attenuation and dispersion of silica-based optical fibers in the optical communication band of 1.3–1.6  $\mu\text{m}$ . Several microwave and optical waveguide technologies have been examined in the THz region. The major challenge of THz waveguide technologies is the relatively strong absorption in most of the conventional waveguide structures, which prevents THz wave transmission over long distances.

### 5.4.1 Theory of Rectangular Waveguides

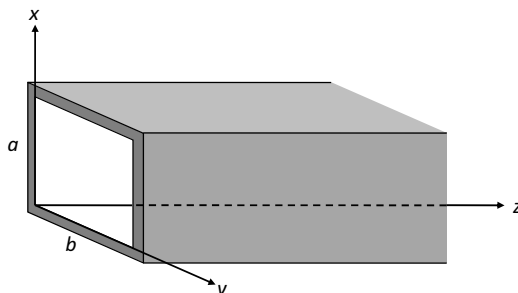


**Fig. 5.16.** Rectangular waveguide

To get a sense of how waves propagate in a waveguide, we look into a metal tube of rectangular shape (Fig. 5.16). The electric and magnetic fields of a monochromatic wave travelling through the waveguide in the positive direction of the z-axis have the generic form

$$\mathbf{E}(x, y, z, t) = \mathbf{E}_0(x, y) e^{i(kz - \omega t)}, \quad (5.24)$$

$$\mathbf{B}(x, y, z, t) = \mathbf{B}_0(x, y) e^{i(kz - \omega t)}, \quad (5.25)$$

where  $\mathbf{E}_0 = E_x \mathbf{e}_x + E_y \mathbf{e}_y + E_z \mathbf{e}_z$  and  $\mathbf{B}_0 = B_x \mathbf{e}_x + B_y \mathbf{e}_y + B_z \mathbf{e}_z$ . Unlike propagation in free space, guided waves, in general, are not transverse, i.e., the longitudinal components  $E_z$  and  $B_z$  do not vanish. Inserting Eqs. 5.24 and 5.25 into Maxwell's equations (Eqs. 2.1, 2.2, 2.3, and 2.4) and manipulating the equations, we obtain the wave equations for  $E_z$  and  $B_z$ :

$$\left[ \frac{\partial^2}{\partial x^2} + \frac{\partial^2}{\partial y^2} + \frac{\omega^2}{c^2} - k^2 \right] E_z(x, y) = 0, \quad (5.26)$$

$$\left[ \frac{\partial^2}{\partial x^2} + \frac{\partial^2}{\partial y^2} + \frac{\omega^2}{c^2} - k^2 \right] B_z(x, y) = 0. \quad (5.27)$$

Noting that these two equations are independent of each other, we can classify guided waves into different types of modes. If  $E_z = 0$  we call the waves transverse electric (TE) modes. Similarly, transverse magnetic (TM) modes have no longitudinal component of the magnetic field,  $B_z = 0$ . A TEM mode has neither electric nor magnetic field in the longitudinal direction. A hollow waveguide, however, does not support TEM modes.

Suppose we are interested in TE modes. We obtain  $B_z(x, y)$  by solving Eq. 5.27, then determine the other components of electric and magnetic fields using the following relations obtained from Maxwell's equations:

$$E_x = \frac{i\omega}{(\omega/c)^2 - k^2} \frac{\partial B_z}{\partial y}, \quad (5.28)$$

$$E_y = \frac{-i\omega}{(\omega/c)^2 - k^2} \frac{\partial B_z}{\partial x}, \quad (5.29)$$

$$B_x = \frac{ik}{(\omega/c)^2 - k^2} \frac{\partial B_z}{\partial x}, \quad (5.30)$$

$$B_y = \frac{i\omega}{(\omega/c)^2 - k^2} \frac{\partial B_z}{\partial y}. \quad (5.31)$$

The general solution of Eq. 5.27 has the form,

$$B_z(x, y) = [A \sin(k_x x) + B \cos(k_x x)] \cdot [C \sin(k_y y) + D \cos(k_y y)], \quad (5.32)$$

where the coefficients  $A$ ,  $B$ ,  $C$ , and  $D$ , and the wavenumbers,  $k_x$  and  $k_y$ , are determined by boundary conditions. Under the assumption that the metal is a perfect conductor, electromagnetic waves vanish inside the material. Accordingly, the electric and the magnetic fields satisfy the boundary conditions that the parallel components of the electric field and the normal component of the magnetic field vanish at the interior surface,  $\mathbf{E}_{||} = 0$  and  $\mathbf{B}_{\perp} = 0$ . Applying the boundary condition  $\mathbf{E}_{||} = 0$  to Eqs. 5.28 and 5.29, we obtain

$$B_z(x, y) = B_0 \cos\left(\frac{m\pi}{a}x\right) \cos\left(\frac{n\pi}{b}y\right), \quad (m, n = 0, 1, 2, \dots). \quad (5.33)$$

Figure 5.17 shows the spatial profile of the field intensity for the low-order TE modes.

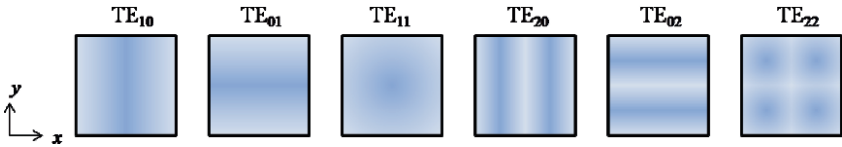


**Fig. 5.17.** Field distribution of TE modes in a cross section of a rectangular waveguide

Inserting Eq. 5.33 into the wave equation, we get the dispersion relation,

$$k = \frac{1}{c} \sqrt{\omega^2 - \omega_{mn}^2}, \quad (5.34)$$

where the cutoff frequency,

$$\omega_{mn} = \pi c \sqrt{\frac{m^2}{a^2} + \frac{n^2}{b^2}}. \quad (5.35)$$

If  $\omega < \omega_{mn}$  the wavenumber  $k$  is imaginary, the wave attenuates exponentially as  $e^{-|k|z}$ . Therefore, the frequency of a travelling wave must be higher than the cutoff frequency. The phase and the group velocities,

$$v_{ph} = \frac{\omega}{k} = \frac{c}{\sqrt{1 - \omega_{mn}^2/\omega^2}}, \quad (5.36)$$

$$v_{gr} = \frac{\partial \omega}{\partial k} = c \sqrt{1 - \omega_{mn}^2/\omega^2}, \quad (5.37)$$

indicate that the waveguide is highly dispersive, especially, near the cutoff frequency.

### 5.4.2 Hollow Metallic Tubes

A comprehensive study has been conducted on rectangular and circular metallic waveguides [136]. THz time-domain spectroscopy (THz-TDS) is employed to measure broadband THz pulses propagating through the 25-mm-long metal tubes of various cross-sectional dimensions. Figure 5.18 shows the waveforms and amplitude spectra of the THz pulses transmitted through (b) a  $250 \mu\text{m} \times 125 \mu\text{m}$  rectangular and (c)  $280 \mu\text{m}$ -diameter circular brass waveguide, with the incoming waves being linearly-polarized single-cycle pulses.

The incoming Gaussian beam is coupled into the rectangular waveguide most efficiently with the lowest-order mode  $\text{TE}_{10}$  when the polarization is parallel to the  $y$ -axis. Consequently, THz wave transmission through this

waveguide is effectively single-mode propagation. The cutoff frequency of the measured spectrum is consistent with the calculated value,  $\omega_{10}=0.6$  THz. The transmitted THz pulse is stretched to  $\sim 15$  ps due to the strong group-velocity dispersion.

Group-velocity dispersion is even stronger in the circular waveguide, through which the pulses are stretched to  $\sim 40$  ps. The interference fringes in the spectrum indicate that the waveguide propagation involves multiple modes. The sharp cutoff at 0.67 THz is close to the calculated cutoff frequency,  $\omega_{11}=0.65$  THz.

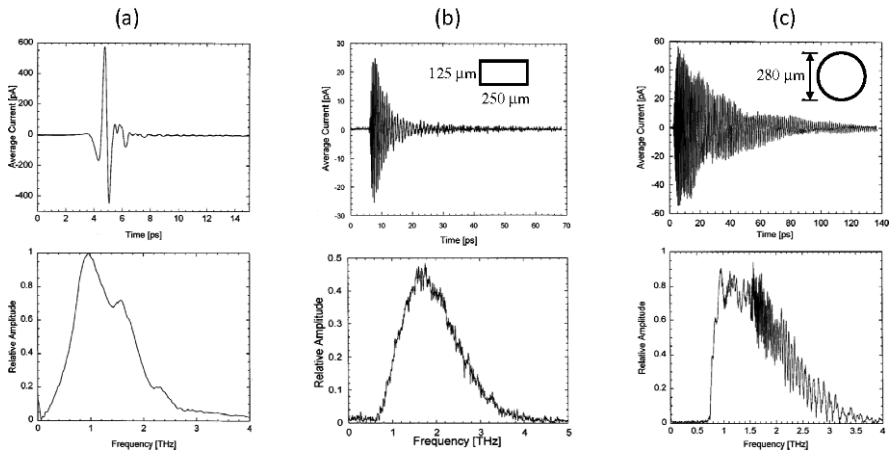


**Fig. 5.18.** THz waveforms and amplitude spectra of (a) the reference, (b) the transmitted pulses through a 25-mm long,  $250\text{ }\mu\text{m}\times 125\text{ }\mu\text{m}$  rectangular brass waveguide, and (c) the transmitted pulses through a 25-mm long,  $280\text{ }\mu\text{m}$ -diameter circular brass waveguide. (Reprinted with permission from [136]. ©2000, American Institute of Physics.)

Before we move on to other waveguide structures, it is worthwhile to review the intrinsic properties of metal-tube THz waveguides pertinent to practical applications. They provide the criteria against which other waveguides are assessed. First, there is a cutoff frequency below which no wave is allowed to propagate. Second, a broadband pulse undergoes a severe waveform distortion due to strong group-velocity dispersion. Third, long-distance propagation is limited by absorption: the absorption coefficient is in the range of  $\sim 1\text{ cm}^{-1}$ . Fourth, incident THz waves efficiently couple into only a few low-order modes: TE<sub>10</sub> and TM<sub>12</sub> modes in a rectangular guide and TE<sub>11</sub>, TE<sub>12</sub>, and TM<sub>11</sub> modes in a circular guide.

### 5.4.3 Dielectric Fibers

A dielectric fiber is a cylindrical waveguide which confines light within the core of the fiber by total internal reflection. The core is surrounded by cladding, layers of material having lower refractive index than that of the core. Most of the dielectric waveguide modes are hybrid, i.e., neither  $E_z$  nor  $B_z$  vanishes. The fundamental mode of a single-mode fiber is the hybrid electric mode  $\text{HE}_{11}$ . The  $\text{HE}_{11}$  mode travelling in the core of refractive index  $n$  with an infinite cladding is expressed as a linearly polarized wave,  $\mathbf{E}_{11}(\rho, \phi)e^{i(kz-\omega t)}$ , and the components of  $\mathbf{E}_{11}(\rho, \phi)$  are given as

$$E_x = E_0 J_0(\beta r), \quad (5.38)$$

$$E_z = E_0 \frac{i\beta}{k} J_1(\beta r) \cos \phi \quad (5.39)$$

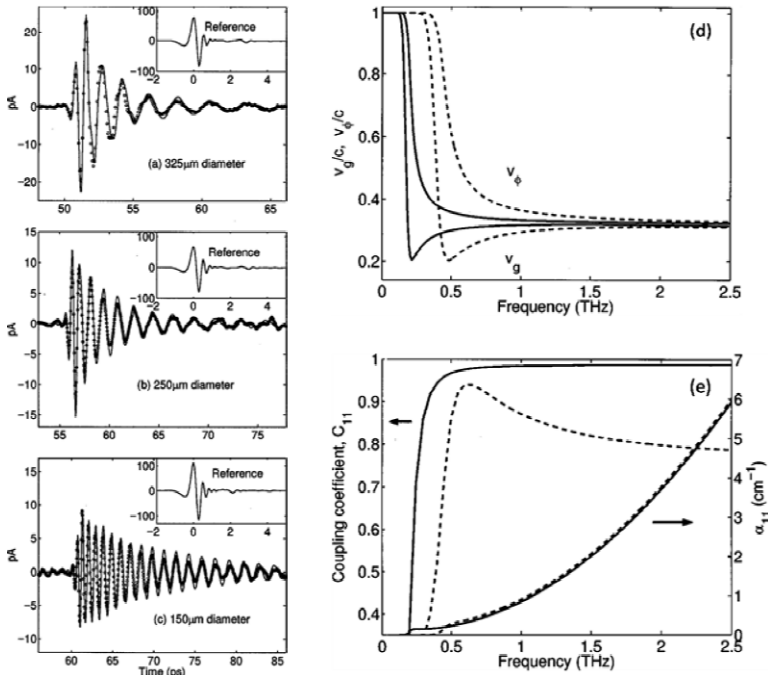


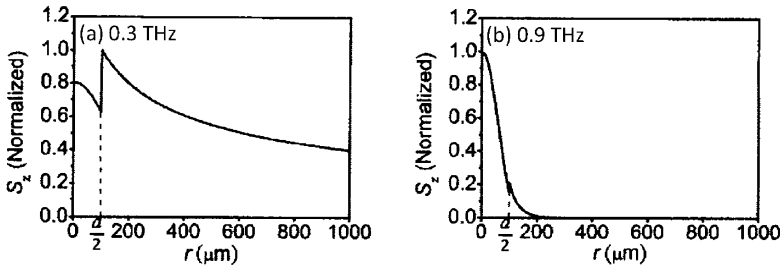
**Fig. 5.19.** Measured (circle) and calculated (solid line) THz pulses transmitted through sapphire fibers of diameter  $a$  and length  $l$ : (a)  $a=325 \mu\text{m}$  and  $l=7.3 \text{ mm}$ , (b)  $a=250 \mu\text{m}$  and  $l=7.8 \text{ mm}$ , and (c)  $a=150 \mu\text{m}$  and  $l=8.3 \text{ mm}$ . The incoming single-cycle pulses are shown in the insets. (d) Calculated group and phase velocities in 325  $\mu\text{m}$ -diameter (solid line) and 150  $\mu\text{m}$ -diameter (dashed line) fibers for  $\text{HE}_{11}$  mode. (e) Coupling coefficient (left axis) and absorption coefficient (right axis) of 325  $\mu\text{m}$ -diameter (solid line) and 150  $\mu\text{m}$ -diameter (dashed line) fibers for  $\text{HE}_{11}$  mode. (Reprinted with permission from [137]. ©2000, American Institute of Physics.)

in terms of cylindrical coordinates, where the dispersion relation,

$$\beta = \sqrt{\frac{n^2\omega^2}{c^2} - k^2}, \quad (5.40)$$

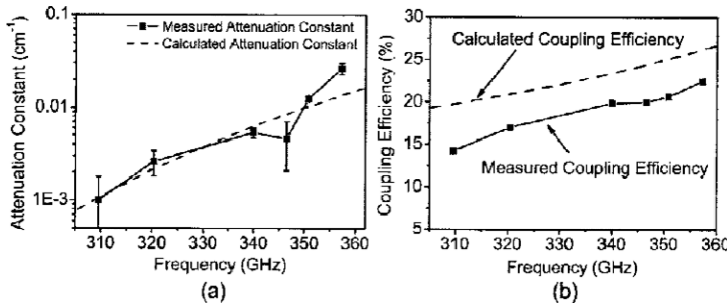
is determined by boundary conditions. Since the HE<sub>11</sub> mode has a linear polarization, an azimuthal symmetry, and a profile very close to a Gaussian distribution, coupling between a free-space beam and the mode can be highly efficient if the mode profile of the incoming beam matches well with that of the HE<sub>11</sub> mode.

Figure 5.19(a)-(c) show broadband THz pulses transmitted through unclad sapphire fibers of three different diameters, 325, 250, and 150  $\mu\text{m}$ , which are comparable to the central wavelength of the pulses [137]. The pulses undergo significant reshaping because the waveguides are strongly dispersive in the spectral range of interest, as shown in Fig. 5.19(d). The frequency-dependent coupling and absorption (Fig. 5.19(e)) also contribute to the pulse reshaping. The solid lines of Fig. 5.19(a)-(c) are calculations obtained by analyzing HE<sub>11</sub> mode propagation in the fibers. The dominance of the HE<sub>11</sub> mode is accounted for by its superior coupling efficiency from free space to waveguide.



**Fig. 5.20.** Radial distribution of the mode intensity profile for a 200- $\mu\text{m}$ -diameter polyethylene fiber at (a) 0.3 and (b) 0.9 THz. (Reprinted from [138].)

Similar to that in hollow metal tubes, attenuation of THz waves in dielectric fibers is too strong for long distance propagation. An interesting approach to reduce the attenuation is to use a fiber with subwavelength core diameter [138]. As shown in Fig. 5.20, if the fiber diameter is significantly smaller than the mode wavelength, only a small fraction of the wave propagates in the core of high loss while the greater part lies in free space. Consequently, the effective attenuation coefficient can be much lower than that of the core material. The attenuation constant of a 200- $\mu\text{m}$ -diameter polyethylene fiber shown in Fig. 5.21(a) is significantly lower than that of polyethylene, in particular, at low frequencies. A drawback of this scheme is that the coupling is relatively inefficient due to substantial mode mismatch (see Fig. 5.21(b)).



**Fig. 5.21.** Measured and calculated (a) absorption coefficient and (b) coupling efficiency of a 200- $\mu\text{m}$ -diameter polyethylene fiber versus frequency. (Reprinted from [138].)

#### 5.4.4 Parallel Metal Plates

An outstanding property of a parallel-plate metal waveguide is that its TEM mode is virtually dispersionless. Figure 5.22 illustrates the TEM mode travelling along the  $z$ -axis within the gap of two metal plates parallel to the  $y$ - $z$  plane. The electric field is linearly polarized in the direction normal to the metal surfaces. The TEM mode is represented in the form of a plane wave,  $\mathbf{E}(z, t) = \mathbf{e}_x E_0 e^{i(kz - \omega t)}$ , inside the waveguide, vanishing elsewhere. The dispersion relation,  $k = \omega/c$ , is identical with that of free space, thus there is no cutoff frequency, and the group and the phase velocities are equal to the speed of light.

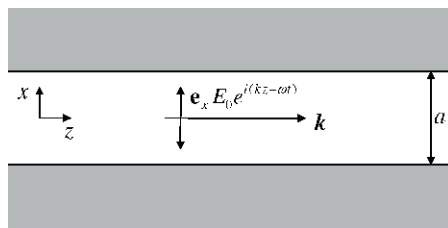


**Fig. 5.22.** TEM mode in parallel metal plates

Figure 5.23(a) shows that single-cycle THz pulses transmitted through a 12.6- and a 24.4-mm-long copper parallel-plate waveguide with a 108- $\mu\text{m}$  gap retain their pulse shapes with little stretching [139]. Plano-cylindrical lenses are attached to the entrance and exit slits to couple the THz beam into and out of the waveguides. The power loss is relatively low compared with metal tubes and dielectric fibers: the amplitude absorption coefficient  $\alpha/2$  is less than 0.2  $\text{cm}^{-1}$  in the broad spectral range from 0.1 to 4.5 THz.

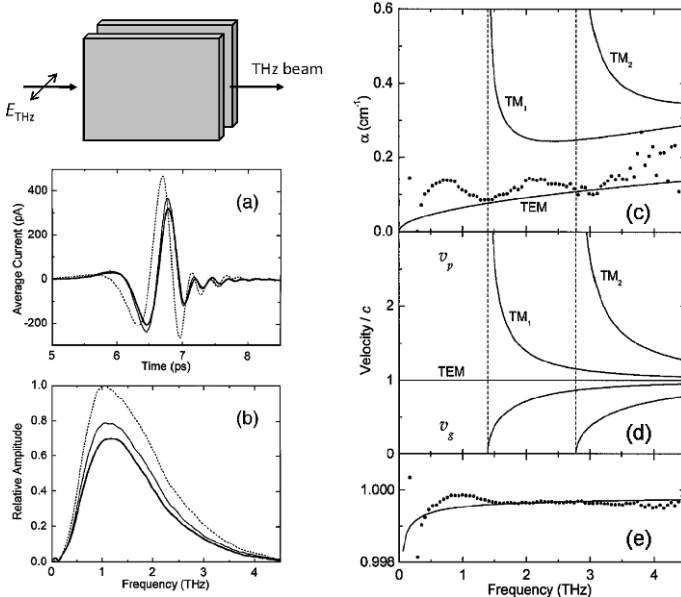


**Fig. 5.23.** (a) Waveforms and (b) spectra of broadband THz pulses transmitted through a 12.6- and a 24.4-mm-long copper parallel-plate waveguide with a 108- $\mu\text{m}$  gap. The dashed lines represent the reference pulses. (c) Amplitude absorption coefficient, (d) phase and group velocity scaled with the speed of light, and (e) the scaled velocity of the TEM mode in the vicinity of unity. Solid lines are the calculations for the first three modes, and the filled circles indicate experimental data. (Reprinted from [139].)

#### 5.4.5 Metal Wires

A fascinating development in guiding THz waves is that a bare metal wire turned out to be an effective waveguide with virtually no dispersion and little attenuation [140]. Electromagnetic waves propagating on a long cylindrical conductor are called surface plasmon waves, whose existence was first predicted by A. Sommerfeld in 1899. The Sommerfeld wave is a radially symmetric TM mode travelling along the cylinder axis. THz surface plasmon polaritons at a metal-dielectric interface are of great interest because of their unique properties applicable to near-field optics and subwavelength optics. A comprehensive review of this subject is featured in section 5.5.3. In the present section, we will focus on guided THz waves on a metal wire.

In the cylindrical coordinate system shown in Fig. 5.24, the electric and magnetic fields of the Sommerfeld wave propagating along the z-axis are expressed as

$$\mathbf{E}(\mathbf{r}, t) = [\mathbf{e}_r E_r(r) + \mathbf{e}_z E_z(r)] e^{i(kz - \omega t)}, \quad (5.41)$$

$$\mathbf{B}(\mathbf{r}, z) = \mathbf{e}_\phi B_\phi(r) e^{i(kz - \omega t)}. \quad (5.42)$$

**E** and **B**, having azimuthal symmetry, are independent of the azimuthal angle  $\phi$ . In the transverse plane, **E** has only a radial component  $E_r(r)$  and **B** has only azimuthal component  $B_\phi(r)$ .

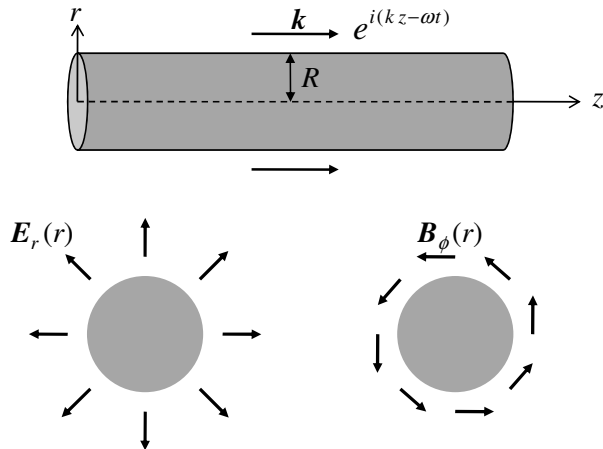


**Fig. 5.24.** Surface plasmon wave travelling on a cylindrical metal wire

The universal wave equation, Eq. 2.15, leads to the wave equation for the longitudinal electric field  $E_z(r)$ :

$$r^2 \frac{d^2}{dr^2} E_z(r) + r \frac{d}{dr} E_z(r) - \beta^2 r^2 E_z(r) = 0, \quad (5.43)$$

where the radial parameter  $\beta$  is associated with the dispersion relations

$$\beta_a^2 = k^2 - \frac{\omega^2}{c^2} \quad (5.44)$$

in free space and

$$\beta_c^2 = k^2 - \epsilon_r \mu_r \frac{\omega^2}{c^2} \cong k^2 - i\mu\sigma\omega \quad (5.45)$$

in a conductor with dielectric constant  $\epsilon_r$ , relative permeability  $\mu_r = \mu/\mu_0$ , and conductivity  $\sigma$ . Solutions of Eq. 5.43 are modified Bessel functions,  $I_0(\beta r)$  and  $K_0(\beta r)$ . Conforming to the fact that surface plasmon waves fade away from the metal surface, a proper expression of  $E_z(r)$  takes the form

$$E_z(r) = \begin{cases} E_c I_0(\beta_c r) & \text{for } r < R \\ E_a K_0(\beta_a r) & \text{for } r > R \end{cases}. \quad (5.46)$$

Using Maxwell's curl equations, 2.3 and 2.4, we obtain the relations of  $E_r$  and  $B_\phi$  with  $E_z$ :

$$E_r(r) = \frac{k}{i\beta^2} \frac{dE_z(r)}{dr}, \quad (5.47)$$

$$B_\phi(r) = \frac{k^2 - \beta^2}{i\omega\beta^2} \frac{dE_z(r)}{dr}, \quad (5.48)$$

where

$$\frac{dE_z(r)}{dr} = \begin{cases} \beta_c E_c I_1(\beta_c r) & \text{for } r < R \\ -\beta_a E_a K_1(\beta_a r) & \text{for } r > R \end{cases}. \quad (5.49)$$

The recurrence relations of the modified Bessel functions,  $I'_0(\xi) = I_1(\xi)$  and  $K'_0(\xi) = -K_1(\xi)$ , are applied to attain Eq. 5.49.

The boundary conditions that  $E_z$  and  $B_\phi$  are continuous at  $r = R$  lead to the transcendental equation,

$$\frac{\epsilon_r}{\beta_c} \frac{I_1(\beta_c R)}{I_0(\beta_c R)} = -\frac{1}{\beta_a} \frac{K_1(\beta_a R)}{K_0(\beta_a R)}, \quad (5.50)$$

from which, and together with

$$\beta_a^2 - \beta_c^2 = (\epsilon_r \mu_r - 1) \frac{\omega^2}{c^2}, \quad (5.51)$$

we can determine  $\beta_a$  and  $\beta_c$ .

Relying on theoretical background, we shall attempt to gain some physical insight into the Sommerfeld wave. The asymptotic expansions of  $I_1(\xi)$  for  $\xi \gg 1$ ,

$$I_1(\xi) \sim \sqrt{\frac{\pi}{2\xi}} e^\xi, \quad (5.52)$$

and the series expansion of  $K_1(\xi)$ ,

$$K_1(\xi) = \frac{1}{\xi} + \dots, \quad (5.53)$$

are useful for understanding its properties. As discussed in section 5.2.3, a THz wave undergoes excessive attenuation in a metal with a typical penetration depth less than  $0.1 \mu\text{m}$ . Consequently, the THz surface plasmon wave propagates almost entirely in free space. A rational ramification of this is that the longitudinal wavenumber  $k$  must be very close to  $\omega/c$ . Eventually, we find  $\beta_a \ll k$  according to Eq. 5.44. As Eq. 5.53 indicates that the mode amplitude is roughly proportional to  $\frac{1}{\beta_a r}$  in free space, the mode is extended into a region where its dimension is much greater than the mode wavelength,  $\lambda = 2\pi/k$ . On the other hand, inside the conductor, the radial parameter  $\beta_c$  has the relation,  $|\beta_c| \sim |\epsilon_r \mu_r| \frac{\omega}{c} \gg k$ , because  $|\epsilon_r \mu_r| \gg 1$ . Assuming the wire radius  $R$  is comparable to or larger than  $\lambda$ , we obtain  $\beta_c R \gg 1$ . Then, the mode amplitude near the metal surface, proportional to  $e^{\beta_c r}$ , attenuates exponentially with the penetration depth,  $|\sqrt{2/\omega\mu\sigma}| \ll \lambda$ . As shown in Fig. 5.25,  $B_\phi(r)$ , continuous at the boundary, extends far and gradually attenuates as  $\sim 1/\beta_a r$

in free space while decaying exponentially within a very short distance  $\sim 1/\beta_c$  inside the conductor. The amplitude of the electric field inside the conductor is significantly smaller than that in free space. Since  $E_z(r)$  is continuous at the boundary, the radial component  $E_r(r)$  is dominant in free space. Virtually, the guided mode is a transverse wave in free space.

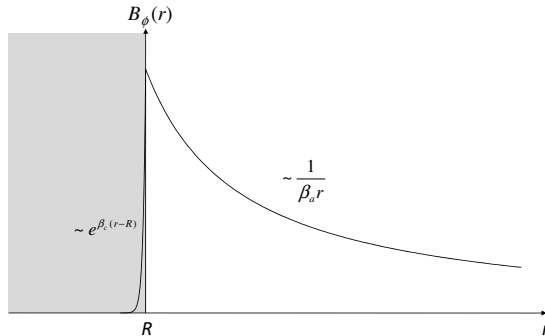


**Fig. 5.25.** Radial distribution of  $B_\phi(r)$

An important question is how the surface plasmon wave attenuates in the propagation direction. We make an estimation of the wavenumber  $k$  assuming the wire is sufficiently thick so that  $R$  is at least several times larger than  $\lambda$ . Under this condition, it is valid that  $I_1(\beta_c R)/I_0(\beta_c R) \approx K_1(\beta_a R)/K_0(\beta_a R) \approx 1$ , then the transcendental equation (Eq. 5.50) is reduced to

$$\beta_c^2 \approx \epsilon_r \mu_r \beta_a^2. \quad (5.54)$$

Inserting Eqs. 5.44 and 5.45 into Eq. 5.54, we obtain

$$k \approx \left( \frac{\epsilon_r \mu_r}{\epsilon_r \mu_r + 1} \right)^{1/2} \frac{\omega}{c} \approx \frac{\omega}{c} + i \frac{\omega^2}{2c^3 \mu \sigma}. \quad (5.55)$$

Here  $k$  is indeed very close to the free space wavenumber  $\frac{\omega}{c}$  since  $\left| \frac{\omega}{2c^2 \mu \sigma} \right| \ll 1$ . The surface wave attenuates in the propagation direction as  $\sim e^{-\alpha z}$  with the absorption coefficient,  $\alpha = \Re \left\{ \frac{\omega^2}{c^3 \mu \sigma} \right\} \ll k$ . For example, it is estimated that  $\alpha \sim 2 \times 10^{-4} \text{ cm}^{-1}$  for a thick copper wire ( $\sigma_0 = 5.96 \times 10^7 \text{ S} \cdot \text{m}^{-1}$ ).

How are these wave parameters affected as the wire radius decreases? The transcendental equation is helpful for a qualitative analysis of this matter. The ratio  $K_1(\beta_a R)/K_0(\beta_a R)$ , bigger than unity for a finite  $R$ , increases as  $R$  is decreased. Hence,  $\beta_a$  and  $\alpha$  increase accordingly. For example, if  $R \sim \lambda \sim 1 \text{ mm}$ ,  $\beta_a$  and  $\alpha$  are roughly one order larger than the values for an infinitely thick wire. Figure 5.26 shows the experimental measurements on THz pulses transmitted through a copper wire waveguide with radius  $R=0.26 \text{ mm}$  [141].

The mode extends several millimeters from the wire axis, and decays inversely with radial distance  $r$ . The absorption coefficient is in the range of  $10^{-3} \text{ cm}^{-1}$ , significantly lower than any other THz waveguide structures.

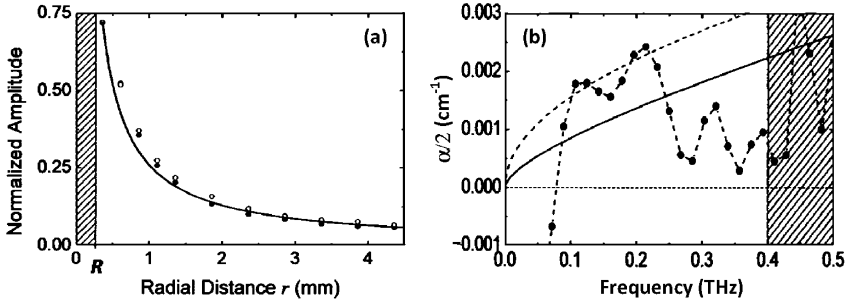


**Fig. 5.26.** Transmitted broadband THz pulses for a copper wire with radius  $R=0.26 \text{ mm}$ . (a) Normalized peak amplitude (open circles) and spectral amplitude (filled circles) at  $0.15 \text{ THz}$ . The data are consistent with the solid line,  $a/r$ . (b) Measured (filled circle) and calculated (solid line) amplitude absorption coefficients. (Reprinted with permission from [141]. ©2005, American Institute of Physics.)

So far, we have discussed guided-wave propagation on a straight wire. What if the wire is bent? How efficiently does the wire waveguide bend and interconnect THz waves? In general, waveguides can transfer waves along straight lines with high efficiency yet even a moderate bending drastically reduces the efficiency due to a strong radiation loss. Metal wires are not an exception in this respect. The experimental data shown in Fig. 5.27 demonstrates that the radiation loss escalates sharply as the radius of curvature,  $R_c$ , is decreased [142]. The amplitude absorption coefficient increases from  $0.03 \text{ cm}^{-1}$  for a straight wire to  $0.15 \text{ cm}^{-1}$  for  $R_c=20 \text{ cm}$ . In a phenomenological model incorporating the radiation loss into the overall attenuation, the attenuation coefficient of a bent wire is expressed as

$$\alpha_{R_c} = \alpha_0 e^{-\gamma R_c}. \quad (5.56)$$

The solid line in Fig. 5.27 fits the data to this model, which suggests that radiation loss is a dominant attenuation mechanism for bent wires.

A fundamental challenge for the wire waveguide scheme is that it is problematic to couple linearly-polarized THz waves into a wire, because the radially-polarized guided mode has a poor spatial overlap with the waves in free space. The coupling method shown in Fig. 5.28 employs a scattering mechanism which focuses linearly-polarized THz radiation onto a wire waveguide [140]. The coupling efficiency of this method, however, is discouragingly low: the upper limit is estimated as  $\sim 0.4\%$  [143]. As a better alternative, Fig. 5.28(b) shows an ingenious technique to improve the coupling efficiency: THz waves are launched directly from a specially designed photoconductive

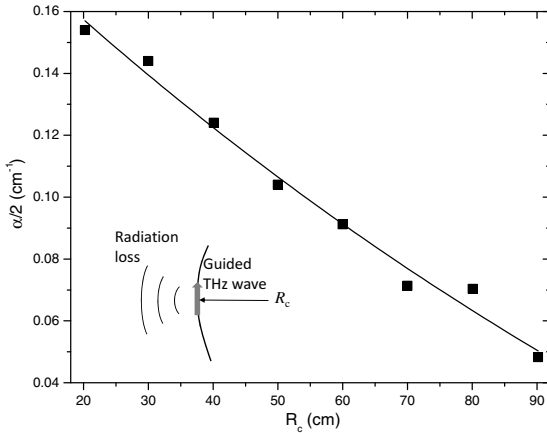


**Fig. 5.27.** Amplitude attenuation coefficient of a 0.9-mm-diameter, 21-cm-long stainless-steel wire as a function of the radius of curvature  $R_c$ . (Data from Ref. [142])

emitter into the metal wire [141, 143]. The radially symmetric photocurrents flowing between the two concentric electrodes produce radially-polarized THz radiation which matches well with the guided-wave mode. A numerical simulation predicts that the coupling efficiency can reach up to 60% [143].

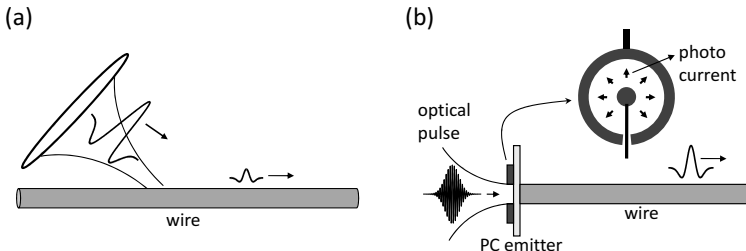


**Fig. 5.28.** (a) Scattering method used to couple linearly-polarized THz waves into a wire waveguide. (b) Direct launching of THz waves into a wire waveguide using a photoconductive emitter with a radially symmetric antenna structure.

## 5.5 Artificial Materials at Terahertz Frequencies

### 5.5.1 Metamaterials

A metamaterial refers to an artificially structured composite that exhibits exotic electromagnetic properties unattainable with naturally occurring ma-

terials. Figure 5.29 illustrates the basic concept behind electromagnetic metamaterials. The metamaterial consists of artificially structured elements embedded in a uniform matrix. As an electromagnetic wave interacts with the metamaterial, whose structural elements are smaller than the wavelength, the material system responds to the the wave like a homogeneous medium. That is, the electromagnetic properties of the metamaterial are characterized by an effective permittivity  $\epsilon(\omega)$ , and an effective permeability  $\mu(\omega)$ , independent of space. It is of great interest that some structural elements of particular design can give rise to extraordinary optical properties that are markedly different from those of the constituent materials. In particular, negative refractive index metamaterials have attracted a great deal of scientific and technological interests. While the peculiar properties of negative refraction were first predicted by Victor Veselago several decades ago [144], these material systems had remained hypothetical until 2000 when a composite medium showed simultaneously negative  $\epsilon$  and  $\mu$  over a band in the microwave range [145]. Since then, metamaterials have been demonstrated over a wide range of the electromagnetic spectrum from radio frequencies [146] to the near-infrared [147], including THz metamaterials [148].

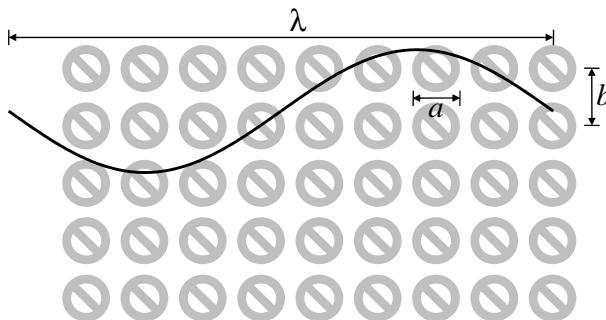


**Fig. 5.29.** Electromagnetic metamaterial

In order to understand the effects of negative refraction, it is necessary to review the basic concepts and theory of the interaction between electromagnetic waves and matter (see section 2.1). The refractive index of an isotropic medium is defined as

$$n(\omega)^2 = \epsilon_r(\omega)\mu_r(\omega), \quad (5.57)$$

where  $\epsilon_r(\omega) = \epsilon(\omega)/\epsilon_0$  and  $\mu_r(\omega) = \mu(\omega)/\mu_0$ , and the refraction of an electromagnetic wave at an interface between vacuum and the medium is governed by Snell's law,

$$\sin \theta = n \sin \theta_r, \quad (5.58)$$

where  $\theta$  is the angle of incidence and  $\theta_r$  is the angle of refraction. All naturally occurring dielectric media have positive  $\epsilon_r$  and  $\mu_r$ , thus  $n^2 > 0$ . Although

Eq. 5.57 implies that  $n$  can be either  $+\sqrt{\epsilon_r \mu_r} (> 0)$  or  $-\sqrt{\epsilon_r \mu_r} (< 0)$ , the boundary conditions at the interface warrant that  $\theta_r$  is positive, and hence  $n$  is positive, too (Fig. 5.30(a)). Because the directions of the electric field  $\mathbf{E}$ , the magnetic field  $\mathbf{B}$ , and the wave vector  $\mathbf{k}$  of an electromagnetic wave in this medium follow the so-called right-hand rule (e.g.,  $\mathbf{E} \parallel \mathbf{e}_x$ ,  $\mathbf{B} \parallel \mathbf{e}_y$ , and  $\mathbf{k} \parallel \mathbf{e}_z$ ), a medium with positive  $n$  is called a right-handed material (RHM). On the other hand, if  $\epsilon_r < 0$  and  $\mu_r < 0$ ,  $\theta_r$  has a negative value which satisfies the the boundary conditions, and thus the medium has a negative refractive index ( $n < 0$ ), and is called a left-handed material (LHM) (Fig. 5.30(a)).

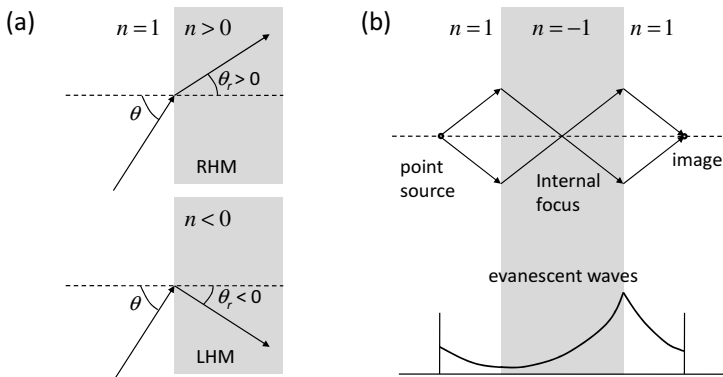


**Fig. 5.30.** (a) Refraction by right-handed and left-handed materials (b) Perfect focusing by a slab of a negative refractive index material

Arguably, the most important application of negative refraction is high-resolution imaging by use of perfect focusing, as shown in Fig. 5.30(b) [149]. The slab of LHM functions as a perfect lens, focusing the near-field as well as the far-field components of the point source. Consequently, the image can have spatial resolution beyond the diffraction limit. Perfect focusing is attainable because the near-field or evanescent components, which rapidly decay in RHMs, grow exponentially in LHMs.<sup>1</sup> Other notable ramifications of negative refraction include the phase velocity being antiparallel to the Poynting vector, the Doppler shift is reversed, and Cherenkov radiation is in the backward direction.

Split-ring resonators (SRRs) are the most commonly used magnetic elements to form a metamaterial. Figure 5.31(a) shows the schematic of an SRR consisting of two concentric bands of nonmagnetic conductor. When an oscillating magnetic field applied to the SRR has a nonvanishing component in

<sup>1</sup> The evanescent waves are characterized by large transverse wave vectors, and thus carry information of the subwavelength-scale variation. The growth of evanescent waves in LHMs does not violate the conservation of energy because no energy is transported by evanescent waves.

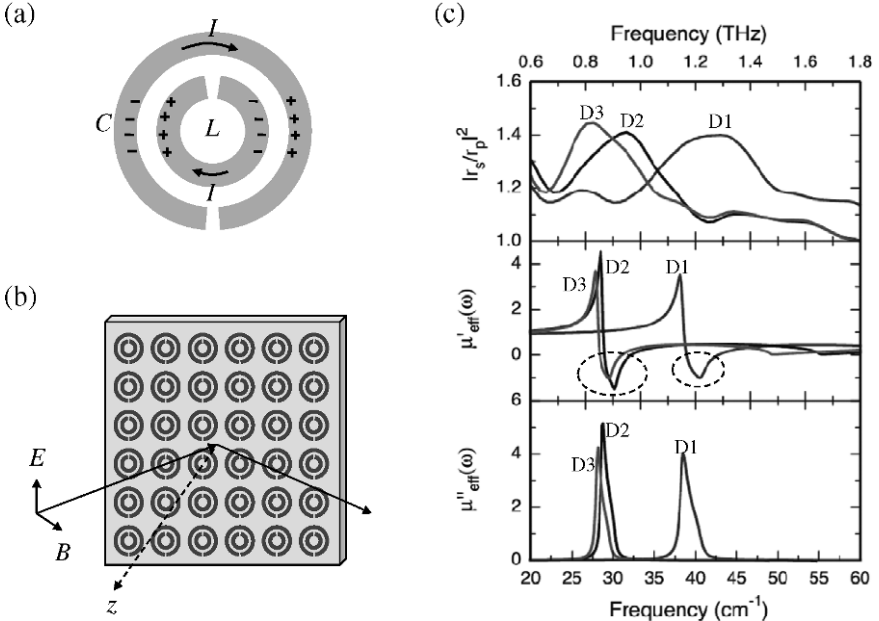


**Fig. 5.31.** Magnetic response of conducting split-ring resonators (SRRs) at THz frequencies. (a) SRR Geometry: equivalent to an LC resonator. (b) Ellipsometry measurements on a two-dimensional SRR array deposited on a dielectric substrate. (c) The ratio of the magnetic to electric response ( $|r_s/r_p|^2$ ) (experiment) and the real ( $\mu'_{\text{eff}}$ ) and imaginary ( $\mu''_{\text{eff}}$ ) magnetic permeability (numerical simulation) for three samples of different sizes (D1 < D2 < D3). (From [148]. Reprinted with permission from AAAS.)

the direction normal to the surface, the changing magnetic field induces currents around the rings and, simultaneously, displacement currents ( $J_D \propto \frac{\partial E}{\partial t}$ ) produced by the accumulating charges flow through the gaps between the rings. Simply put, the SRR functions as an LC resonator of two capacitors and a double-ring inductor in series, driven by magnetic fields. Accordingly, the frequency-dependent effective permeability has the form

$$\mu_{\text{eff}}(\omega) = \mu'_{\text{eff}}(\omega) + i\mu''_{\text{eff}}(\omega) = 1 - \frac{F\omega^2}{\omega^2 - \omega_0^2 + i\gamma\omega}, \quad (5.59)$$

where  $\mu'$  and  $\mu''$  are the real and imaginary part of the permeability,  $F$  is the oscillator strength depending on the SRR geometry,  $\omega_0 \sim 1/\sqrt{LC}$  is the resonant frequency, and  $\gamma$  is the decay rate of the resonator due to resistive loss. The magnetic response of SRRs can be observed by the ellipsometry measurements shown in Fig. 5.31(b). As  $B_z \neq 0$ , the reflectivity coefficient  $r_s$  of s-polarization depends on the magnetic permeability of the SRR, while  $r_p$  exhibits no magnetic response because  $B_z = 0$  for p-polarization. The top

panel of Fig. 5.31(c) shows the ratio of the s- and p-pol reflectivities of three SRR samples as a function of frequency [148]. The broad peaks of the spectra are centered at the resonant frequencies scaling with sample dimensions:  $\omega_1 > \omega_2 > \omega_3$  as  $D1 < D2 < D3$ . A numerical simulation, using the sample parameters as input, exhibits a strong diamagnetic behavior where  $\mu'_{\text{eff}}(\omega)$  has negative values near and above the resonant frequencies.

Electrical response can also be harnessed by artificial structures. In fact, it has been known for a long time that an array of conducting wires exhibit negative permittivity in a specific spectral range determined by its geometry. The frequency-dependent permittivity has the form

$$\epsilon_{\text{eff}}(\omega) = 1 - \frac{\omega_p^2}{\omega^2 - \omega_0^2 + i\gamma\omega}, \quad (5.60)$$

with the plasma frequency,

$$\omega_p^2 = \frac{n_{\text{eff}}e^2}{m^*}. \quad (5.61)$$

It gives the flexibility of controlling the electrical response, in that the effective electron density  $n_{\text{eff}}$  and mass  $m^*$ , as well as the resonant frequency  $\omega_0$ , are governed by the geometry of the wire array. A three-dimensional structure of negative refractive index metamaterial can be constructed by alternatingly stacking layers of SRR arrays and conducting wire arrays [150].

An interesting application of metamaterials is to control and manipulate THz waves by use of active metamaterial devices. Figure 5.32(a) depicts the electric resonator element and the equivalent circuit of an active THz device. The parallel strips at the center function as capacitors, and the loops on the left- and right-hand sides as inductors. Because the loops are wound in opposite directions, there is no magnetic response from this element. The element is deposited on a n-GaAs layer on top of a SI-GaAs substrate. When no bias is applied between the element and the substrate, the split gap is shorted because of the relatively conductive substrate. Lacking capacitance, the element does not exhibit any resonant behavior. A reverse bias, however, depletes electrons in the n-GaAs layer, and hence the resistivity  $R_d$  between the split gap shoots up sharply, which makes the element act like an electric resonator. Figure 5.32(b) sketches the experimental arrangement for transmission measurements by THz-TDS. The active device consists of a planar array of metamaterial elements. All the elements are connected to a common electrode to serve as a Schottky gate. The active control of THz waves is shown in Figure 5.32(c). The polarization of the incident THz radiation is perpendicular to the connecting wires. In the transmission spectra of Fig. 5.32(c-1), the resonance dips at 0.72 and 1.65 THz grow as the gate bias is increased. The corresponding permittivity shown in Fig. 5.32(c-2) demonstrates significant modulations of the electric response of the device. As a comparison, the transmission spectra of a blank device with no metamaterial element (Fig. 5.32(c-3)) are featureless and independent of the gate bias.

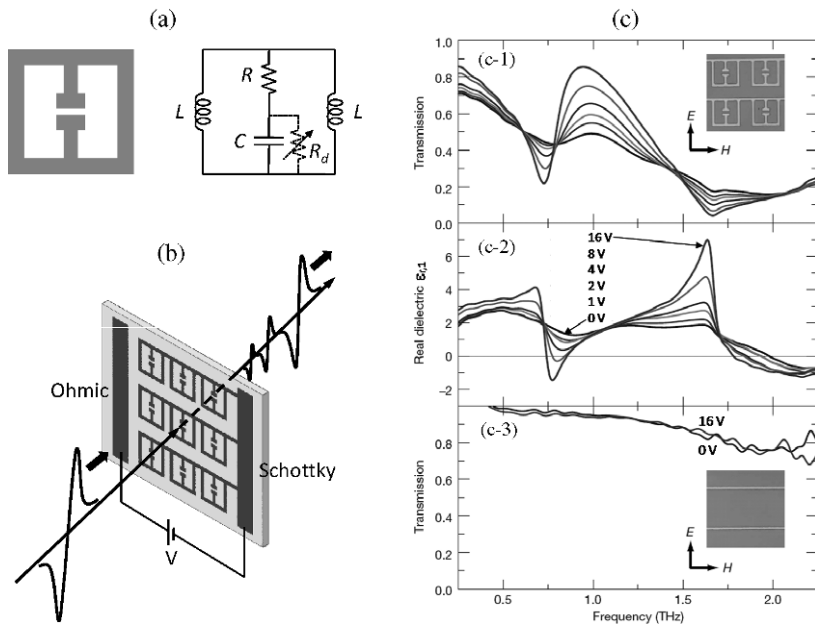


**Fig. 5.32.** Active control of THz waves by metamaterial devices. (a) Schematic of the structural element and the equivalent circuit. (b) Transmission measurement by THz-TDS (c) Switching performance for various gate biases. (c-1) Frequency dependent transmission and (c-2) the corresponding permittivity for gate biases from 0 to 16 V. (c-3) Transmission spectra of a blank device with no metamaterial element for gate biases of 0 and 16 V. (Reprinted by permission from Macmillan Publishers Ltd: Nature [151], ©2006.)

### 5.5.2 Photonic Crystals

A crystal is formed as a periodic array of atoms. In a crystalline conductor, electrons move freely, experiencing no scattering with atoms. An insulator has an energy band gap in which no electronic state is allowed. These unique electrical properties of crystals are governed by the wave nature of electrons subject to a periodic potential. Analogous to electron systems, a photonic crystal has a periodic lattice structure whose constituent media have distinctive dielectric constants. Figure 5.33 illustrates examples of one-, two-, and three-dimensional photonic crystals.

When an electromagnetic wave interacts with a photonic crystal whose lattice constant is comparable to the wavelength, the refracted and reflected waves from the lattice elements undergo strong interference, and ultimately form a standing wave called an electromagnetic mode. A group of modes form a continuous energy band. If the interference is completely destructive for

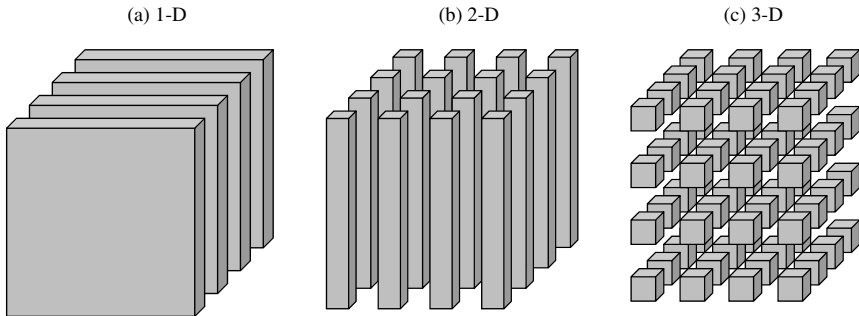


**Fig. 5.33.** Representative structures of 1-D, 2-D, and 3-D photonic crystals.

some frequency range, corresponding modes are forbidden in the photonic crystal, and the forbidden energy range is called a photonic band gap.

Naturally, we can ask what the photonic bandgap structures are good for. From a practical point of view, photonic crystals are an excellent base system upon which we can build compact, integrated optical circuits. As we discussed briefly in section 5.4.5, radiation losses from even a slight bend in nominal waveguides are significant as well as unavoidable. Waveguides built in a photonic crystal, however, can transport light with little or no loss at sharp bends. Therefore, together with other optical components, switching, mixing, and modulating optical signals can be accomplished in a small scale device based on photonic crystals.

A photonic crystal of dielectric media is characterized solely by a periodic dielectric function conforming to the relation

$$\epsilon_r(\mathbf{r}) = \epsilon_r(\mathbf{r} + \mathbf{u}) \quad (5.62)$$

for all Bravais lattice vectors  $\mathbf{u} = n_1\mathbf{a}_1 + n_2\mathbf{a}_2 + n_3\mathbf{a}_3$ , where  $\mathbf{a}_1$ ,  $\mathbf{a}_2$ , and  $\mathbf{a}_3$  are the lattice vectors, and  $n_1$ ,  $n_2$ , and  $n_3$  are arbitrary integers. The electromagnetic modes in the photonic crystal take the generic form (see section 2.1)

$$\mathbf{H}(\mathbf{r}, t) = \mathbf{H}(\mathbf{r})e^{-i\omega t}, \quad (5.63)$$

$$\mathbf{E}(\mathbf{r}, t) = \frac{i}{\omega\epsilon_0\epsilon_r(\mathbf{r})}\nabla \times \mathbf{H}(\mathbf{r}, t), \quad (5.64)$$

where the spatial mode function  $\mathbf{H}(\mathbf{r})$  is determined by the wave equation

$$\nabla \times \left[ \frac{1}{\epsilon_r(\mathbf{r})} \nabla \times \mathbf{H}(\mathbf{r}) \right] = \frac{\omega^2}{c^2} \mathbf{H}(\mathbf{r}). \quad (5.65)$$

Solving the wave equation together with the periodic boundary condition, we can obtain eigenvalues  $\omega(\mathbf{k})$  and eigenfunctions  $\mathbf{H}_k(\mathbf{r})$ , where  $\mathbf{k}$  is a Bloch wave vector lying in the Brillouin zone. The periodic boundary condition warrants an infinite number of discrete eigenvalues  $\omega_n(\mathbf{k})$  for each  $\mathbf{k}$ , and  $\omega_n(\mathbf{k})$  is a

continuous function for a given band index number  $n$ . The band structure of a photonic crystal refers to the information contained in the dispersion relation  $\omega_n(\mathbf{k})$ . The wave equation is scalable, thus the basic concepts and theoretical framework are applicable to the entire electromagnetic spectrum.

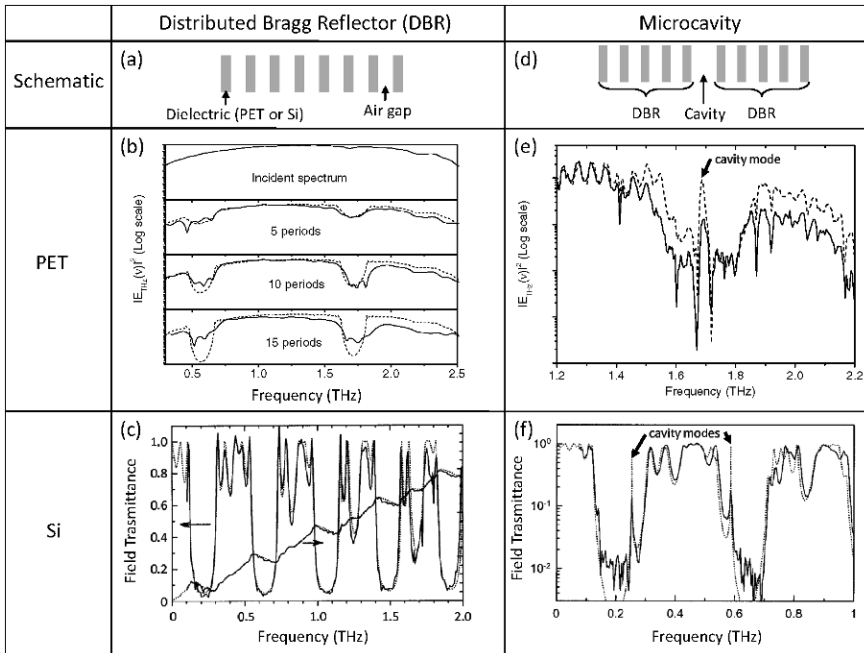


**Fig. 5.34.** 1-D photonic crystal devices at THz frequencies: distributed Bragg reflectors and microcavities. (a), (d) Schematics (b), (e) Spectra of broadband THz pulses transmitted through the components made of polyethylene terephthalate (PET). The dotted-lines depict theoretical calculations. One period of the structures consists of a 75- $\mu\text{m}$  PET film ( $n=1.65$ ) and a 125- $\mu\text{m}$  air gap. The three DBR samples have 5, 10, and 15 periods. The 1-D resonant cavity consists of two DBRs with 2.5 periods of PET/air separated by a 250- $\mu\text{m}$  air gap. (Data from Ref. [152]) (c), (f) Field transmittance of Si ( $n=3.42$ ) components. The dotted-lines depict theoretical calculations. The DBR has three 100- $\mu\text{m}$  Si wafers separated by 350- $\mu\text{m}$  air layers. The air gap in the resonant cavity is 548- $\mu\text{m}$  thick. (Reprinted from [153].)

Although they have not been called by this name, 1-D photonic crystals have been used as basic optical components such as mirrors, filters, and resonant cavities for a long time. Figure 5.34 shows a few examples of 1-D photonic crystal devices at THz frequencies. The devices are made of either polyethylene terephthalate (PET) or high-resistive silicon (Si). A distributed Bragg reflector (DBR) consists of multiple layers of alternating dielectric media, and has stopbands in which propagation of light is forbidden. Figure 5.34(b) and

(c) show stopbands of the PET and the Si DBRs in their transmission spectra measured by THz-TDS. The resonant cavities are formed by two DBRs separated by an air gap, and have cavity modes in the middle of the DBR stopbands. The cavity modes of the PET and Si microcavities are shown in Figure 5.34(e) and (f).

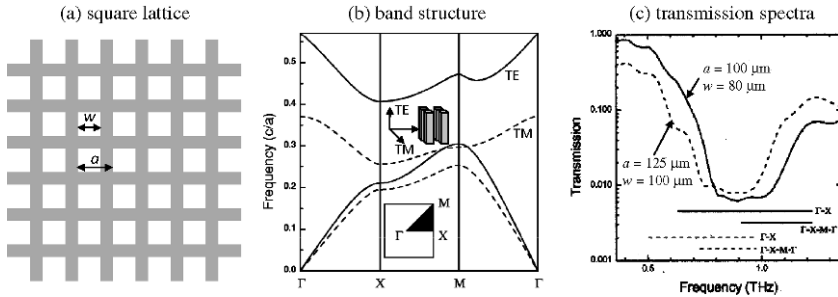


**Fig. 5.35.** (a) 2-D photonic crystal with square lattice.  $w$  is the hole width and  $a$  is the lattice constant. (b) Photonic band structure of Si ( $n=3.41$ ) for  $w/a=0.8$ . Solid and dashed lines indicate TE and TM bands, respectively. The unit of frequency is  $c/a$ , where  $c$  is the speed of light in free space. The inset shows the irreducible Brillouin zone of a 2-D square lattice. (c) Transmission spectra for TE-polarized light propagating in the  $\Gamma$ -X direction: solid lines for  $a=100 \mu\text{m}$ ,  $w=80 \mu\text{m}$  and dotted lines for  $a=125 \mu\text{m}$ ,  $w=100 \mu\text{m}$ . The horizontal lines correspond to the calculated 2-D TE band gap and the TE band gap in the  $\Gamma$ -X direction. (Reprinted with permission from [154]. ©2003, American Institute of Physics.)

Microfabrication techniques used for semiconductor devices have been employed to fabricate photonic crystals of high precision. 2-D photonic crystals with a square lattice, shown in Fig. 5.35(a), were made of high-resistivity Si using deep reactive ion etching [154]. Figure 5.35(b) depicts the photonic band structure of the square lattice ( $w/a = 0.8$ ) for TE and TM polarizations. The TE polarization is perpendicular to the plane of the lattice, and the TM polarization is parallel to the plane. The TE and TM band gaps are  $0.10c/a$  and  $0.004c/a$ , respectively. Figure 5.35(c) shows the spectra of TE-polarized THz radiation for the samples of  $a=125 \mu\text{m}$  and  $a=100 \mu\text{m}$ . The stopbands of the two samples are clearly shown and consistent with the numerical calculations of the TE band gap.

In general, no confinement is imposed on light in the vertical direction of a 2-D photonic crystal. A parallel-plate waveguide can be employed to accomplish vertical confinement. As we discussed in section 5.4.4, a TEM mode in a parallel-plate waveguide is not only bound in a narrow gap of conducting plates, but also is dispersionless. Figure 5.36(a) illustrates the schematic of a 2-D photonic bandgap structure embedded in a parallel-plate waveguide. The square lattice consists of SU-8 polymer ( $n = 1.7$ ) cylinders.

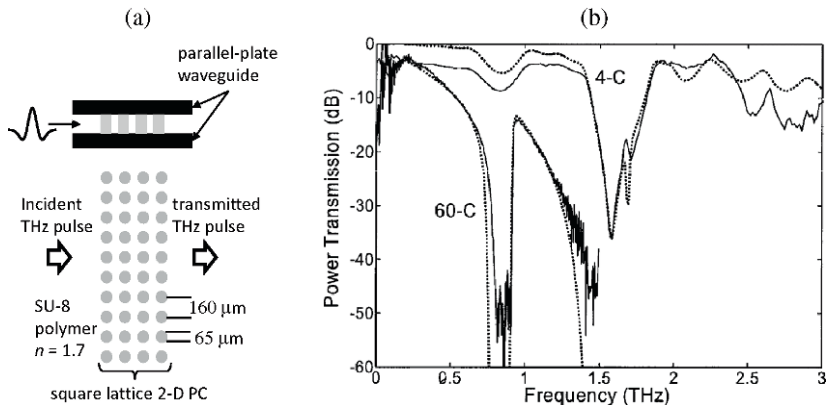


**Fig. 5.36.** (a) Schematic diagram of the THz transmission measurements of a 2-D photonic crystal, a square lattice of SU-8 polymer cylinders ( $n=1.7$ ), embedded in a parallel-plate waveguide. The dielectric cylinders are 65- $\mu\text{m}$  diameter and 70- $\mu\text{m}$  high, and the lattice constant is 160  $\mu\text{m}$ . (b) Transmission spectra for the 4-column and 60-column samples. The dotted lines show theoretical calculations. (Reprinted from [155].)

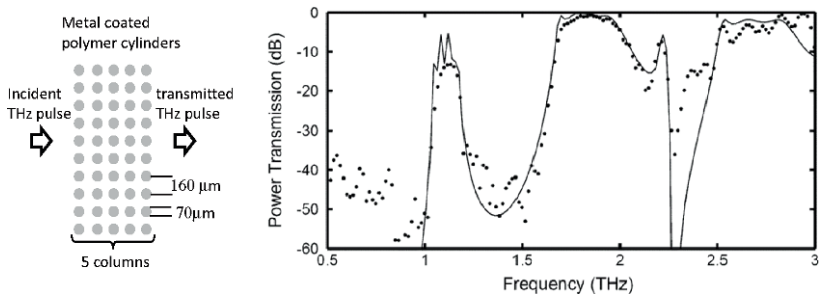
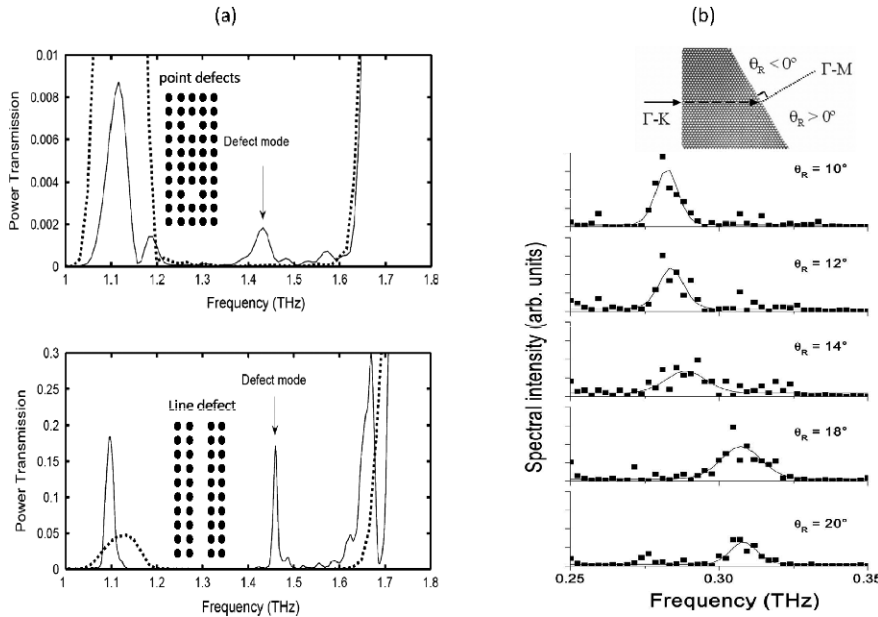


**Fig. 5.37.** Measured (dots) and calculated (solid line) transmission spectra of a 2-D metallic photonic crystal of square lattice ( $a=160 \mu\text{m}$ ). The sample has five columns of gold coated cylinders (70- $\mu\text{m}$  diameter and 80- $\mu\text{m}$  height). (Reprinted from [156]. ©2007 IEEE)

Figure 5.36(b) shows the transmission spectra of 4-column and 60-column samples. SU-8 is relatively lossy at THz frequencies ( $\alpha \cong 18\nu_{THz} \text{ cm}^{-1}$ , where  $\nu_{THz}$  is in THz), and hence absorption is discernible. It becomes stronger at higher frequencies and/or with more columns. The spectral features of the stopbands are consistent with the theoretical calculations depicted as dotted lines.

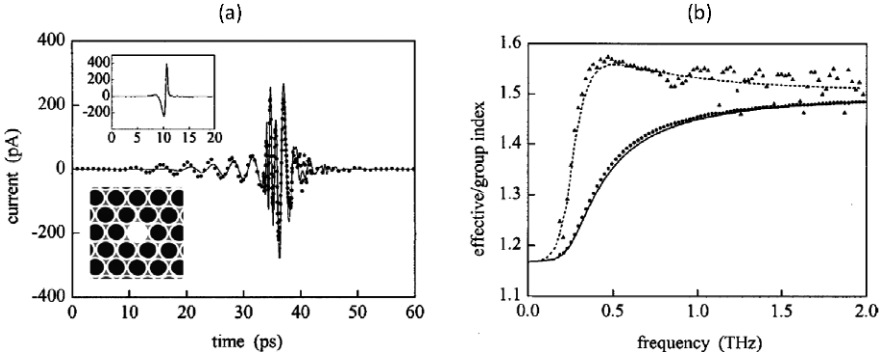
The transmission loss can be reduced by coating the dielectric cylinders with metal. Metallic photonic crystals are impractical in the optical region because of large ohmic losses, but the effects are much smaller in the THz regime.

Figure 5.37 shows the transmission spectrum of a 2-D metallic photonic crystal. The gold coating on the cylinders ( $\sim 2.5\text{-}\mu\text{m}$  thick) is considerably thicker than the penetration depth of gold at THz frequencies ( $\delta < 0.1\text{ }\mu\text{m}$  at 1 THz), thus the photonic bandgap structure is considered to be purely metallic.



**Fig. 5.38.** THz devices based on 2-D metallic photonic crystal (a) Defect modes of two samples with point defects and a line defect. The square lattice ( $a=160\text{ }\mu\text{m}$ ) consists of gold coated cylinders ( $70\text{-}\mu\text{m}$  diameter and  $80\text{-}\mu\text{m}$  height). (Reprinted from [156]. ©2007, IEEE) (b) Anomalous refraction from a superprism containing a hexagonal array ( $a=400\text{ }\mu\text{m}$ ) of circular holes ( $360\text{-}\mu\text{m}$  diameter) in a  $305\text{-}\mu\text{m}$  thick Si wafer. (Reprinted from [157].)

A few examples of THz devices based on 2-D photonic crystals in a parallel-plate waveguide are shown in Fig. 5.38. Defects in a photonic crystal give rise to defect modes. Figure 5.38(a) shows the sharp features of defect modes of two square lattice samples containing point defects and a line defect, respectively. An experimental demonstration of the superprism effect is shown in Fig. 5.38(b). Since a photonic crystal is, in general, highly dispersive due to its complex band structure, a prism made of photonic crystal can exhibit a drastic change of refraction angle with a slight change of incident angle. This phenomenon is called the superprism effect. Certain superprism structures even allow negative refraction. The spectrum of diffracted THz radiation shown in Fig. 5.38(b) displays an abrupt spectral shift as the angle is varied over a small range, the characteristic superprism effect.



**Fig. 5.39.** Guided-wave propagation in a THz photonic crystal fiber. (a) Measured (dots) and calculated (solid line) THz waveform after propagating through a 2-cm long plastic photonic crystal fiber. The insets show the measured input waveform and an optical micrograph of the cross-section of the photonic crystal fiber with a high index defect. (b) Effective (dots: measured, solid line: calculated) and group (triangles: measured, dashed: calculated) indices. (Reprinted with permission from [158]. ©2002, American Institute of Physics.)

Another type of THz devices utilizing 2-D photonic crystals is photonic crystal fibers. The inset at the bottom of Fig. 5.39 shows the cross-section of a photonic crystal fiber made of HDPE tubes [158]. A high-index defect of HDPE is placed at the center of the structure. THz waves propagate along the defect in the vertical direction of the photonic crystal. The lattice constant is  $500 \mu\text{m}$ , and the tube thickness is  $50 \mu\text{m}$ . Figure 5.39(a) shows a transmitted THz waveform through a 2-cm-long sample. The input waveform is shown in the inset at the top. The effective and group indices of the photonic crystal fiber are obtained from the data. The measured values agree well with theoretical calculations, as shown in Fig. 5.39(b).

Fabrication of 3-D photonic crystals has been demonstrated in several different ways. A few notable techniques are summarized in Fig. 5.40. A relatively simple method is to stack up thin layers on which a 2-D structure is etched off. Overall symmetry of the resulting 3-D structure depends on the relative orientations and displacements between the layers as well as the 2-D structure. Figure 5.40(a) gives an example [159]. Conventional KOH etching is employed to construct a grating structure on  $100\text{-}\mu\text{m}$ -thick (110) silicon wafers, taking off  $185\text{-}\mu\text{m}$ -wide gaps separated by  $50\text{-}\mu\text{m}$ -wide stripes. Four layers in the stacking direction make up one period: adjacent layers are 90 degrees off and alternate layers are displaced by a half-period of the grating. The transmission spectrum of a 16-layer sample shows a clear bandgap centered at  $0.45 \text{ THz}$ . The band edges agree well with the theoretical calculation indicated by the arrows. Figure 5.40(b) shows a construction scheme based on an epitaxial technique, which is capable of fabricating very fine structures. The scanning electron microscope image depicts a 3-D photonic crystal of

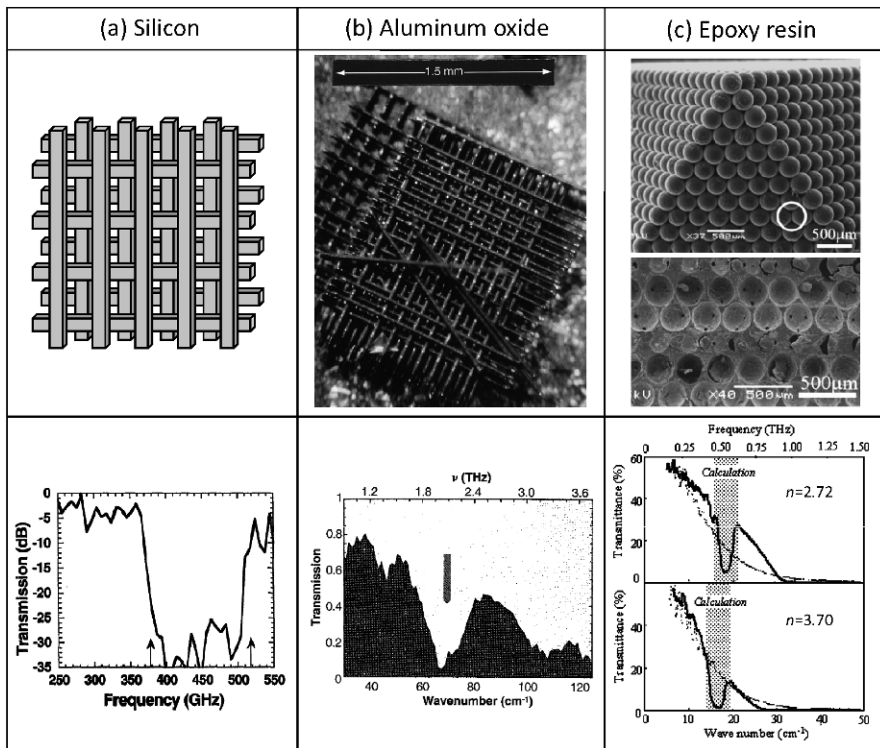


**Fig. 5.40.** Structures and transmission spectra of 3-D photonic crystals (a) Stack of micromachined (110) silicon wafers. Each layer (thickness of 100- $\mu\text{m}$ ) consists of 50- $\mu\text{m}$ -wide rods separated by 185- $\mu\text{m}$ -wide gaps. Four layers in the stacking direction make up one period. The transmission spectrum at normal incidence is for a 16-layer sample. The arrows indicate calculated band-edges. (Reprinted from [159].) (b) Photonic crystals of aluminium oxide fabricated by laser-assisted chemical vapor deposition. Each layer consists of 40- $\mu\text{m}$ -diameter rods separated by 133  $\mu\text{m}$ . The transmission spectrum at normal incidence shows a stopband at 2 THz. (From [160]. Reprinted with permission from AAAS.) (c) Photonic crystals of epoxy resin fabricated by inverting metal sphere templates. Scanning electron microscope images of the copper sphere (diameter of 267  $\mu\text{m}$ ) template and the cross section of an inverse crystal composed of air-spheres are shown in the top panel. Transmission spectra of two 13-layer samples for the waves propagating in the [111] direction are shown in the lower panel. The crystals have a dielectric constants of 2.72 (top) and 3.70 (bottom). Dotted lines represent bulk media without the crystal. (Reprinted with permission from [161]. ©2004, American Institute of Physics.)

aluminium oxide fabricated by laser-assisted chemical vapor deposition. The structure is composed of layers of parallel rods of 40- $\mu\text{m}$ -diameter separated by 133- $\mu\text{m}$ , forming a face-centered tetragonal lattice. Growing vertically, each rod is directly built from chemical vapors with the aid of a 2-mW, 488-nm

laser beam focused on a spot size 5  $\mu\text{m}$  in diameter. Figure 5.40(c) demonstrates a self-assembling technique. The scanning electron microscope (SEM) image at the top shows a metal template in which copper spheres of 267- $\mu\text{m}$  diameter are packed into an fcc lattice (lattice constant of 378  $\mu\text{m}$ ). A reverse crystal of a dielectric medium is constructed by submerging the template in curable epoxy and etching away the copper spheres after curing. The transmission spectra of two samples ( $n=2.72$  and 3.70) exhibit stopbands around 0.5 THz.

### 5.5.3 Plasmonics

Plasmonic devices make up an important part of THz applications. Some of the THz devices discussed in previous sections—bandpass filters (section 5.3.3), wire-grid polarizers (section 5.3.4), and metal-wire waveguides (section 5.4.5)—actually rely on phenomena associated with THz surface plasmons at metal-insulator interfaces. Phenomenological models were provided to account for how the devices function. In this section, we shall look into the underlying physical processes of surface plasmons at THz frequencies, and then discuss a few exquisite phenomena applicable to high-resolution imaging and nonlinear optics.

Surface plasmons are collective oscillations of free electrons at the boundary between a conducting and a dielectric media. The undulating surface charge density accompanies electromagnetic modes trapped at the interface. The strong coupling between a photon and a surface plasmon is called a surface plasmon polariton. Figure 5.41(a) illustrates the coupling between an electromagnetic wave and a charge density fluctuation. Due to the surface charges, the electric fields have components normal to the surface at the boundary, while the magnetic fields are transverse. The fields decay exponentially with distance from the surface as shown in Fig. 5.41(b).

As the surface plasmon propagates in the  $x$  direction, the electric and magnetic fields in the two media are expressed as

$$\mathbf{E}_d(\mathbf{r}, t) = (\mathbf{e}_x E_{d,x} + \mathbf{e}_z E_{d,z}) e^{-\kappa_d z} e^{i(k_x x - \omega t)}, \quad (5.66)$$

$$\mathbf{H}_d(\mathbf{r}, t) = \mathbf{e}_y H_d e^{-\kappa_d z} e^{i(k_x x - \omega t)}, \quad (5.67)$$

$$\mathbf{E}_m(\mathbf{r}, t) = (\mathbf{e}_x E_{m,x} + \mathbf{e}_z E_{m,z}) e^{\kappa_m z} e^{i(k_x x - \omega t)}, \quad (5.68)$$

$$\mathbf{H}_m(\mathbf{r}, t) = \mathbf{e}_y H_m e^{\kappa_m z} e^{i(k_x x - \omega t)}, \quad (5.69)$$

where  $\mathbf{E}_d$  and  $\mathbf{H}_d$  are in the dielectric medium ( $z > 0$ )), and  $\mathbf{E}_m$  and  $\mathbf{H}_m$  in the metal ( $z < 0$ )). The surface wave is characterized by the wavenumbers  $k_x$ ,  $\kappa_d$ , and  $\kappa_m$  for a given frequency  $\omega$ . The generic wave equation, Eq. 2.15, yields the dispersion relations,

$$k_x^2 - \kappa_d^2 = \epsilon_d \frac{\omega^2}{c^2}, \quad (5.70)$$

$$k_x^2 - \kappa_m^2 = \epsilon_m \frac{\omega^2}{c^2}, \quad (5.71)$$

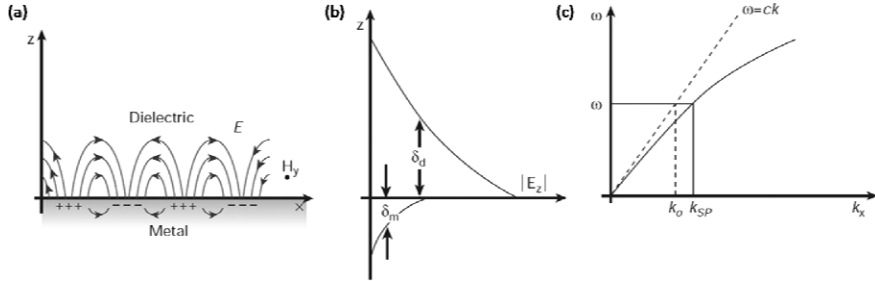


**Fig. 5.41.** Surface plasmons at the interface between a metal and a dielectric. (a) Electromagnetic wave coupled to surface charge density fluctuation. (b) Exponential decay of  $|E_z|$  with decay lengths  $\delta_d$  in the dielectric medium and  $\delta_m$  in the metal. (c) Dispersion curve for surface plasmons (Reprinted by permission from Macmillan Publishers Ltd: Nature [162], ©2003.)

where  $\epsilon_d$  and  $\epsilon_m$  are the dielectric constants of the dielectric and the conducting media. Here we assume that the materials are nonmagnetic. Combining these two equations, we get the relation of the ratio  $\kappa_d/\kappa_m$  expressed in terms of  $k_x$  and  $\omega$ :

$$\frac{\kappa_d^2}{\kappa_m^2} = \frac{k_x^2 - \epsilon_d \omega^2/c^2}{k_x^2 - \epsilon_m \omega^2/c^2}. \quad (5.72)$$

Applying Maxwell's equation, Eq. 2.3, we obtain the relations between  $E_x$  and  $H_y$ :

$$H_{d,y} = -i\epsilon_0 \frac{\epsilon_d \omega}{\kappa_d} E_{d,x}, \quad (5.73)$$

$$H_{m,y} = i\epsilon_0 \frac{\epsilon_m \omega}{\kappa_m} E_{m,x}. \quad (5.74)$$

$H_y$  and  $E_x$ , which parallel to the surface, are continuous at the boundary. The boundary conditions lead to

$$\frac{\epsilon_d}{\epsilon_m} = -\frac{\kappa_d}{\kappa_m}. \quad (5.75)$$

Substituting Eq. 5.75 into Eq. 5.72, we obtain the dispersion relation of surface plasmons,

$$k_x = \frac{\omega}{c} \left( \frac{\epsilon_d \epsilon_m}{\epsilon_d + \epsilon_m} \right)^{1/2}. \quad (5.76)$$

As shown in Fig. 5.41(c), the surface plasmon wavenumber  $k_{SP}$  is always greater than that of the free-space wavenumber  $k_0$  for a given frequency  $\omega$ . This momentum mismatch means that surface plasmons are nonradiative, and, conversely, free-space radiation cannot directly excite them.

Figure 5.42 sketches a typical scheme used to couple light to a surface mode, which utilizes evanescent waves at an interface of dielectric media to

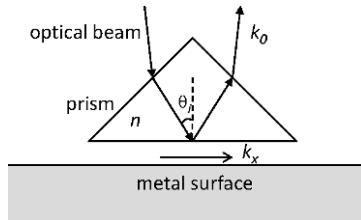


**Fig. 5.42.** Schematic for coupling light to a surface mode by use of evanescent waves at a prism-air interface

circumvent the momentum mismatch between surface plasmons and free-space radiation. With the angle of incidence  $\theta_i$  beyond the critical angle of incidence ( $\theta_c = \sin^{-1} \frac{1}{n}$ ), the optical beam undergoes total internal reflection, which gives rise to an evanescent wave at the prism-air interface. Since  $n \sin \theta_i > 1$ , the evanescent wave can couple to a surface plasmon wave provided that  $k_{SP} = k_x$ , where  $k_x = nk_0 \sin \theta_i (> k_0)$ .

Substituting Eq. 5.76 into Eqs. 5.70 and 5.71, we obtain

$$\kappa_d^2 = -\frac{1}{\epsilon_m + 1} \frac{\omega^2}{c^2}, \quad (5.77)$$

$$\kappa_m^2 = -\frac{\epsilon_m^2}{\epsilon_m + 1} \frac{\omega^2}{c^2}, \quad (5.78)$$

We assume that the dielectric medium is air, i.e.,  $\epsilon_d = 1$ . In the THz regime,  $\epsilon_m$  is mostly imaginary and  $|\epsilon_m| \gg 1$  (see section 5.2.3), thus the attenuation lengths  $\delta_d$  and  $\delta_m$  have the relations,

$$\delta_d = \frac{1}{\Re[\kappa_d]} \cong \frac{\sqrt{|\epsilon_m|}}{\sqrt{2\pi}} \lambda_0 \gg \lambda_0, \quad (5.79)$$

$$\delta_m = \frac{1}{\Re[\kappa_m]} \cong \frac{1}{\sqrt{2|\epsilon_m|}\pi} \lambda_0 \ll \lambda_0, \quad (5.80)$$

where  $\lambda_0 = 2\pi/k_0$ .  $\delta_m$  is virtually identical to the skin depth of the metal. It is noteworthy that  $k_x \approx k_0$ , that is, surface plasmons on a flat metal surface propagate at velocities near the speed of light. Eq. 5.79 indicates that the surface modes at THz frequencies extend into the dielectric medium with distances of many wavelengths. Using  $|\epsilon_m| \sim 10^6$  for common metals (see section 5.2.3), we estimate  $\delta_d \sim 10$  cm at THz frequencies. Propagation of THz surface waves on a metal surface have been observed in experimental studies [163, 164]. The measured attenuation length  $\delta_d$  in air is  $\sim 1$  cm, considerably shorter than the theoretical prediction. This indicates the difficulty of establishing and maintaining the large spatial extent of surface modes in realistic arrangements.

Plasmonics is of great interest in the optical regime, because surface modes at optical frequencies are confined to a small region of subwavelength scale,

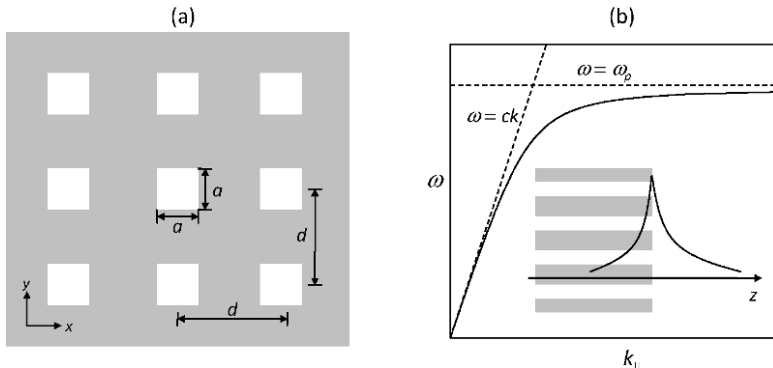


**Fig. 5.43.** Spoof surface plasmons on a structured surface [165]. (a) Perfect conductor with a square-hole lattice. (b) Dispersion curve for spoof surface plasmons. Inset shows the effective evanescent field of a surface mode.

which results in nanoscale spatial resolution and drastic field enhancement. The subwavelength confinement, however, is obtained only at frequencies near the plasma frequency, which is in the ultraviolet in most metals. In order to circumvent the limitation of low-frequency waves, THz plasmonic devices employ structured surfaces to localize and manipulate surface modes. A simple example is shown in Fig. 5.43 [165]. The structured surface is composed of a perfect conductor perforated with a square-hole array. The holes and their spacings are much smaller than the wavelength of radiation,  $a < d \ll \lambda$ , such that electromagnetic responses of the structure can be described by effective permittivity ( $\epsilon_x = \epsilon_y = \epsilon_{||}$  and  $\epsilon_z$ ) and permeability ( $\mu_x = \mu_y = \mu_{||}$  and  $\mu_z$ ) [165].

It is easy to evaluate the  $z$ -axis electromagnetic response of the structured material. Electrons can move freely inside a perfect conductor, and thus it is infinitely susceptible to external electric and magnetic fields, i.e.,  $\epsilon = \mu = \infty$ . No restriction is yet imposed on electron motions in the  $z$ -axis, thus  $\epsilon_z = \mu_z = \infty$ . When it comes to the in-plane responses, calculations based on the effective medium model yield

$$\mu_{||} = \mu_0 \left( \frac{8a^2}{\pi^2 d^2} \right) \quad (5.81)$$

and

$$\epsilon_{||} = \epsilon_0 \frac{\pi^2 d^2}{8a^2} \left( 1 - \frac{\omega_p^2}{\omega^2} \right), \quad (5.82)$$

where the effective plasma frequency  $\omega_p$  is defined as

$$\omega_p = \frac{\pi c}{a}. \quad (5.83)$$

It is notable that  $\omega_p$  is equivalent to the cutoff frequency of the square waveguide (see Eq. 5.35). While propagation of electromagnetic waves is forbidden below the cutoff frequency, exponentially decaying fields can exist near the opening of the waveguide (see section 5.4.1). Consequently, the holes permit effective homogeneous fields to penetrate into the effective medium for a finite distance, yet electric and magnetic fields are completely excluded from the perfect conductor. The penetration depth depends on the in-plane wavenumber  $k_{\parallel}$  and frequency  $\omega$ :

$$\delta_S = \left( k_{\parallel}^2 - \frac{\omega^2}{c^2} \right)^{-1/2}. \quad (5.84)$$

Applying boundary conditions together with the effective dielectric constant, we obtain the dispersion relation for the surface mode,

$$k_{\parallel}c^2 = \omega^2 + \left( \frac{64a^4}{\pi^4 d^4} \right) \frac{\omega^4}{\omega_p^2 - \omega^2}. \quad (5.85)$$

The dispersion curve is shown in Fig 5.43(b). It has the identical form of a typical dispersion relation for surface plasmons. The term *Spoof surface plasmon* was coined referring to surface plasmons on a structured surface. The frequencies near  $\omega_p$  are associated with wavenumbers of large magnitude, and hence surface plasmons can be confined to a small area of the structured surface.

In this simple example, the effective plasma frequency is determined by the structural geometry and not by the intrinsic properties of the base material. This seminal property is generally applicable to any structured surface. An important consequence is that subwavelength confinement of surface plasmons is achievable in the low-frequency region by adjusting the effective plasma frequency to be near the radiation frequency of interest.

A fascinating phenomenon attributed to surface plasmons is that exceptionally high optical transmission is achievable through a periodic array of subwavelength-scale holes in a metal film in certain frequency bands [166]. The enhancement of transmission is associated with the photonic bands of surface plasmons formed by the periodic structure. At a resonant frequency, incident light matches its momentum to that of a surface plasmon together with the lattice momentum. The surface plasmon mode builds constructive interference, and radiates coherently into the other side of the conducting layer. The transmission, normalized by the ratio of hole area to the total area, can exceed unity at resonant frequencies. As we discussed in section 5.3.3, the resonantly enhanced transmission has been utilized for bandpass filters in the THz regime [131, 132]. A phenomenological model of resonant antennas was introduced to account for the extraordinary transmission. The concept of spoof surface plasmons gives insight into the underlying mechanisms of this extraordinary phenomenon.

It is instructive to examine the square hole array of Fig. 5.43(a) a little further. The periodic pattern on the metal surface gives rise to the formation

of photonic bands of surface plasmons, supplying them with crystal momenta,

$$\mathbf{q} = l q_x \mathbf{e}_x + m q_y \mathbf{e}_y, \quad l, m = 0, \pm 1, \pm 2, \dots, \quad (5.86)$$

where  $q_x = q_y = 2\pi/d$ . Incident light impinging on the surface can couple to surface plasmon modes with the momentum matching condition,

$$\mathbf{k}_{SP} = \mathbf{k}_{\parallel} + \mathbf{q}, \quad (5.87)$$

where  $\mathbf{k}_{\parallel}$  is the component of the incident photon's wave vector parallel to the surface.

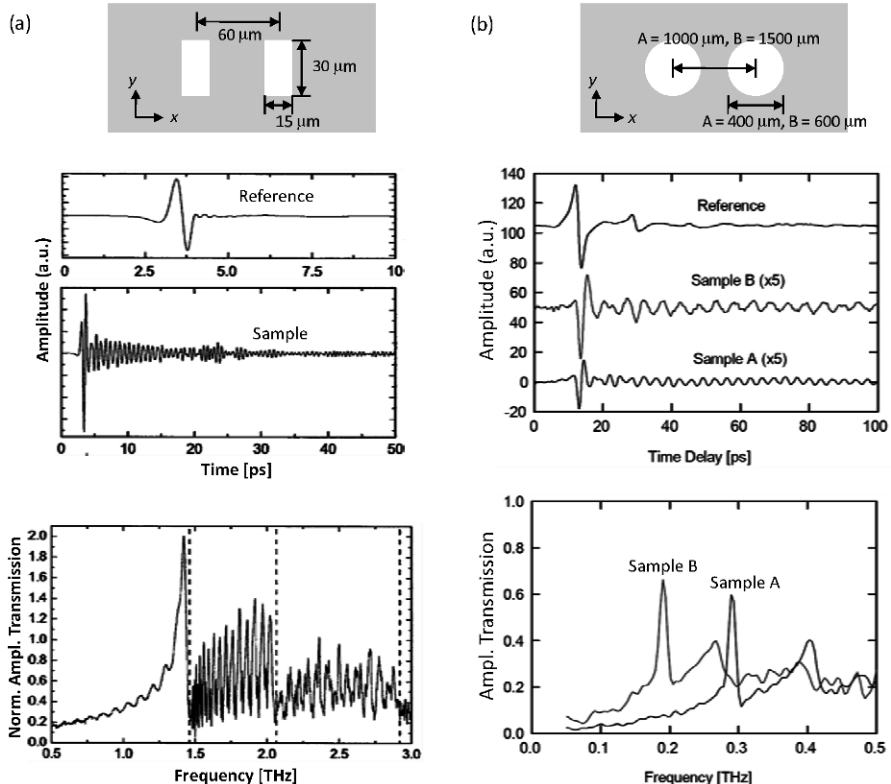


**Fig. 5.44.** Transmission resonances through a periodic array of subwavelength holes. (a) Rectangular hole array. Hole size is  $15 \mu\text{m} \times 30 \mu\text{m}$ , and the grating period is  $60 \mu\text{m}$ . (Reprinted with permission from [167]. ©2004, American Physical Society.) (b) Circular hole array. Hole diameter is  $400$  and  $600 \mu\text{m}$ , and grating period is  $1000$  and  $1500 \mu\text{m}$  for sample A and B, respectively. (Reprinted from [168].)

Figure 5.44 demonstrates experimental observations of transmission resonances at THz frequencies for periodic hole arrays on metal films [167, 168].

The transmission measurements were performed at normal incidence, and hence  $k_{\parallel} = 0$ . Consequently, the resonances occur at integral surface plasmon modes:  $\mathbf{k}_{SP} = \mathbf{q}$ . The rectangular hole array (hole dimension,  $15 \mu\text{m} \times 30 \mu\text{m}$ , grating period,  $60 \mu\text{m}$ ) is constructed on a  $0.25\text{-}\mu\text{m}$ -thick Al film deposited on a Si wafer (Fig. 5.44(a)), and the circular hole array (sample A: hole diameter of  $400 \mu\text{m}$ , grating period of  $1000 \mu\text{m}$ ; sample B: hole diameter of  $600 \mu\text{m}$ , grating period of  $1500 \mu\text{m}$ ) is perforated on a  $75\text{-}\mu\text{m}$ -thick free-standing stainless steel film (Fig. 5.44(b)). The temporal waveforms of the incident and the transmitted THz pulses were measured by THz-TDS. The transmitted THz pulses have long tails of surface plasmon resonances, lasting a few hundred picoseconds. Subsequently, the transmission spectra contain strong resonance peaks. The rectangular hole array has a strongly enhanced transmission at  $1.46 \text{ THz}$ , which corresponds to the first integral surface plasmon mode of  $(l, m) = (\pm 1, 0)$ . The normalized amplitude transmission,  $T \cong 2.0$ , (power transmission is  $\sim 4.0$ ) at the resonant frequency is much greater than unity. The spectrum also shows the  $(\pm 1, \pm 1)$  mode resonance at  $2.06 \text{ THz}$ . The resonances of the circular hole arrays ( $\sim 0.33 \text{ THz}$  and  $\sim 0.46 \text{ THz}$  for sample A,  $\sim 0.2 \text{ THz}$  and  $\sim 0.28 \text{ THz}$  for sample B) correspond to  $(\pm 1, 0)$  and  $(\pm 1, \pm 1)$  modes.

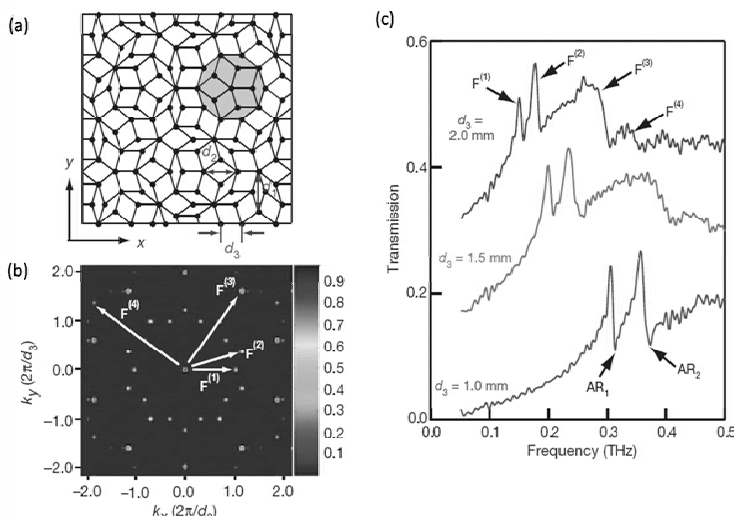


**Fig. 5.45.** Resonantly enhanced transmissions through circular holes patterned on a 2-D quasicrystal lattice structure. (a) A Penrose quasicrystal exhibiting local five-fold rotational symmetry (shaded area) with apertures at the vertices. The hole diameter is  $400 \mu\text{m}$ , and the ratio of hole area to the total area is  $\sim 0.12$ . (b) Geometrical structure factor of the quasicrystal. The reciprocal vectors,  $\mathbf{F}(i)$ , which exhibit ten-fold rotational symmetry, are assigned. (c) Transmission spectra of three Penrose type quasicrystal perforated films with different rhomb side lengths,  $d_3$ . (Reprinted by permission from Macmillan Publishers Ltd: Nature [169], ©2007.)

An interesting twist is that metal films with aperiodic hole arrays can also exhibit resonantly enhanced transmission. Figure 5.45(a) depicts a hole array patterned with a Penrose quasicrystal lattice having local five-fold rotational symmetry. The sample is a 75- $\mu\text{m}$ -thick stainless steel film, the hole diameter is 400  $\mu\text{m}$ , and the ratio of hole area to the total area is  $\sim 0.12$ . Figure 5.45(b) shows the geometrical structure factor of the quasicrystal calculated by the Fourier transform. It displays ten-fold rotational symmetry. The circular spots indicate the reciprocal vectors,  $\mathbf{F}(i)$ , satisfying the relation  $e^{i\mathbf{F}_i \cdot \mathbf{R}} = 1$ , where  $\mathbf{R}$  is a lattice vector. Figure 5.45(c) shows the transmission spectra of three samples having different lattice constants,  $d_3=2000$ , 1500, and 1000  $\mu\text{m}$ . The spectra exhibit transmission resonances corresponding to the reciprocal vectors,  $\mathbf{F}(1)$ ,  $\mathbf{F}(2)$ , and  $\mathbf{F}(3)$ .

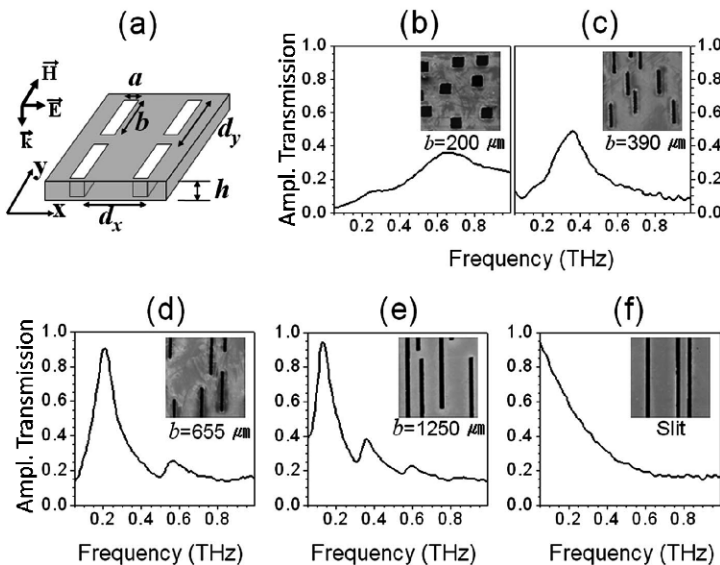


**Fig. 5.46.** (a) Schematic of a 2-D array of rectangular holes of width  $a$  and length  $b$ . The hole positions are randomized. (b)-(f) Amplitude transmission spectra, at normal incidence, of the random arrays of holes with  $a=70 \mu\text{m}$  and  $b=200$ , 390, 655, 1250, and 20000  $\mu\text{m}$ , respectively. Insets are SEM images of the random arrays. (Reprinted with permission from [170]. ©2007, American Physical Society.)

Surprisingly, even a single hole can support resonant transmission, depending solely upon its shape. Figure 5.46 shows examples of shape-dependent transmission resonances [170]. Each sample is composed of a 2-D array of randomly located rectangular holes. The polarization of incident THz radiation is perpendicular to the long side of the holes (Fig. 5.46(a)). Transmitted THz pulses at normal incidence are measured by THz-TDS. While the transmission spectrum of the array of square holes features a weak and broad peak

(Fig. 5.46(b)), the arrays of rectangular holes exhibit sharp resonances determined by the long-side length,  $b$ , of rectangles. The fundamental shape resonance occurs at  $\omega \approx \pi c/b$ , the cutoff frequency of the rectangular waveguide, which is consistent with the effective medium model. The amplitude transmissions of Fig. 5.46(d)-(f) are near unity at the resonances. With the ratio of hole coverage  $\sim 0.12$  and  $b/a=9.4$ , the amplitude enhancement factor reaches up to 8, which confirms the theoretical prediction for a single rectangular hole,  $3b/\pi a \cong 9$  [171].

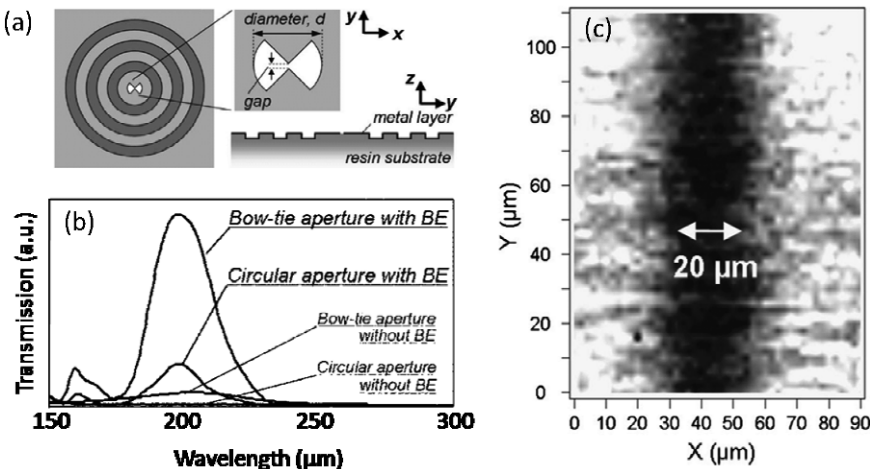


**Fig. 5.47.** THz imaging with subwavelength resolution by use of a metallic bull's eye (BE) structure. (a) Schematic diagram of a bow-tie aperture centered at the BE structure ( $E$ -field  $\parallel y$ -axis). (b) Calculated transmission spectra for bow-tie and circular aperture with and without the BE. The aperture diameter and gap are 50  $\mu\text{m}$  and 6  $\mu\text{m}$ , respectively. The BE consists of six periodic concentric grooves: the depth is 13  $\mu\text{m}$  and the period is 132  $\mu\text{m}$ . The structure is patterned on a resin substrate with  $n=1.5$  and is covered by a 2- $\mu\text{m}$ -thick gold film. (c) Near-field image of a 20- $\mu\text{m}$ -wide Cr pattern at the wavelength of 207  $\mu\text{m}$  (1.45 THz). (Reprinted with permission from [172]. ©2006, American Institute of Physics.)

Figures 5.47 and 5.48 show exemplary schemes to confine THz surface plasmons in a subwavelength scale [172, 173]. The periodic Bull's eye structure of Fig. 5.47(a) enhances the THz transmission through an aperture at the center. The transmission spectra shown in Fig. 5.47(b) indicate that the enhancement factor exceeds one order of magnitude and that the bow-tie aperture is much more efficient than the circular one. Figure 5.47(c) shows the near-field image of a 20- $\mu\text{m}$ -wide Cr strip deposited on a resin substrate taken with a bow-tie aperture with a bull's eye at the wavelength of 207  $\mu\text{m}$ . The spatial resolution of the image is 12  $\mu\text{m}$  corresponding to  $\lambda/17$ . Figure 5.48 shows that subwavelength focusing is achievable by use of a periodically corrugated metallic

cone. Surface plasmons are guided on the conical wire and superfocused at the tip of the cone.

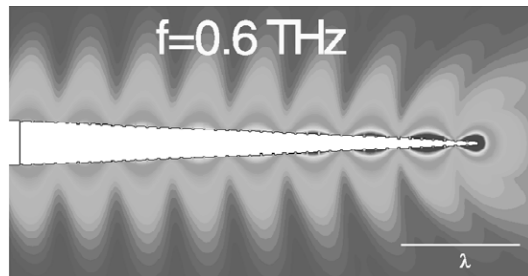


**Fig. 5.48.** Subwavelength focusing of THz surface plasmons on a corrugated cone. The length of the cone is 2 mm. The groove depth and period are 5  $\mu\text{m}$  and 50  $\mu\text{m}$ , respectively. The cone radius varies from 100 to 10  $\mu\text{m}$ . The contour plot represents the  $E$ -field amplitude on a logarithmic scale of two orders of magnitude. (Reprinted with permission from [173]. ©2006, American Physical Society.)

## 5.6 Terahertz Phonon-Polaritons

In ionic crystals electromagnetic waves are strongly coupled to polar lattice vibrations near optical phonon resonances (see section 2.2.4). A phonon-polariton refers to a quasiparticle, resulting from strong coupling between a photon and an optical phonon. In noncentrosymmetric crystals, phonon-polaritons can be excited by femtosecond optical pulses via optical rectification, or, more precisely, impulsive stimulated Raman scattering. This is the same mechanism of THz generation we discussed in section 3.3. When a polariton wave impinges on a crystal/air interface, its electromagnetic component is coupled into air, and the transmitted part emerges as THz radiation in free space.

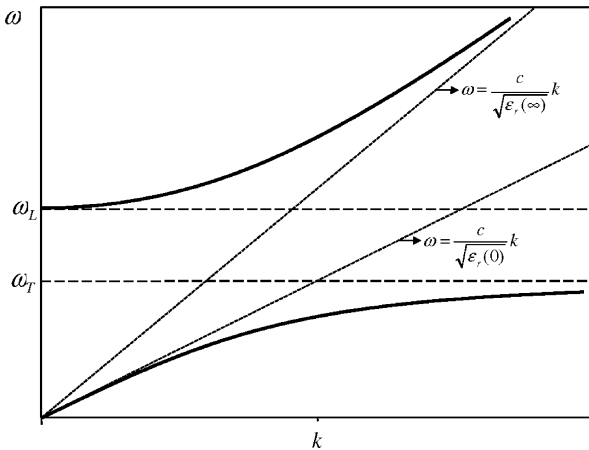
In a spectral region where an optical phonon mode is dominant, a dielectric constant  $\epsilon_r(\omega)$  for an ionic crystal is given as

$$\epsilon_r(\omega) = \epsilon_r(\infty) + \frac{\epsilon_r(\infty) - \epsilon_r(0)}{\omega^2/\omega_T^2 - 1}, \quad (5.88)$$

where  $\omega_T$  is the transverse-optical (TO) phonon frequency. Transverse electromagnetic waves can propagate only if the dispersion relation,

$$k = \frac{\omega}{c} \sqrt{\epsilon_r(\omega)}, \quad (5.89)$$

is satisfied. Figure 5.49 shows the phonon-polariton dispersion relation. The longitudinal-optical (LO) phonon frequency  $\omega_L$  has a simple relation with  $\omega_T$ :

**Fig. 5.49.** Phonon-polariton dispersion relation

$$\omega_L = \sqrt{\frac{\epsilon(0)}{\epsilon(\infty)}} \omega_T. \quad (5.90)$$

The straight lines indicate the dispersion of uncoupled phonon and photon modes. On the high-frequency side, upper-branch polariton mode become photon-like and its propagation is characterized with dielectric constant  $\sqrt{\epsilon(\infty)}$ . As  $\omega \rightarrow 0$ , the lower-branch polariton mode behaves like an electromagnetic wave propagating at  $c/\sqrt{\epsilon(0)}$ . In the regions near  $\omega_T$  and  $\omega_L$  both polariton modes combine photon and phonon properties.

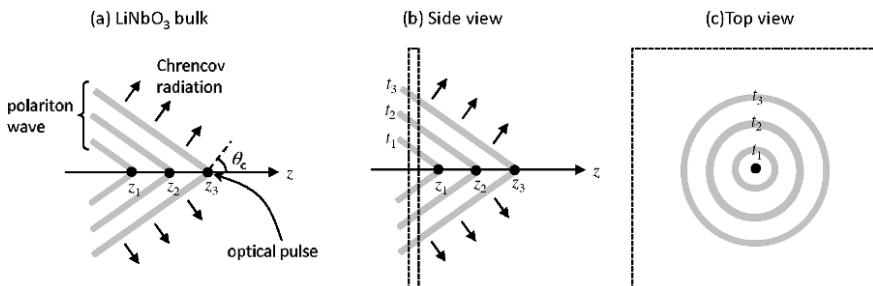


**Fig. 5.50.** (a) Polariton wave generated by a femtosecond pulse passing through a  $\text{LiNbO}_3$  crystal. The black circles indicate a femtosecond optical pulse at different positions  $z_1$ ,  $z_2$ , and  $z_3$ , and the gray lines depict wavefronts of Cherenkov radiation. The Cherenkov angle  $\theta_c$  is  $64^\circ$ . (b) Side and (c) top view of the polariton propagation in the  $xy$ -plane.

Owing to their high optical transparency and strong nonlinearity, lithium niobate ( $\text{LiNbO}_3$ ) and lithium tantalate ( $\text{LiTaO}_3$ ) crystals have been used to study optical excitation and detection of phonon-polaritons. Consider a femtosecond optical pulse propagating through a  $\text{LiNbO}_3$  or  $\text{LiTaO}_3$  crystal, which impulsively creates a THz nonlinear polarization via optical rectification (Fig. 5.50(a)). It is important to note that optical group velocity is significantly higher than THz phase velocity in these crystals. If the optical beam size is smaller than the wavelengths of THz radiation, the THz polarization behaves like a point source of a polariton wave which propagates through the crystal in the form of Cherenkov radiation. In a plane normal to the direction of optical pulse propagation, the Cherenkov cone forms an outgoing circular wave like one created by a pebble dropped into a pond, as shown in Fig. 5.50(b) and (c). Due to the huge velocity mismatch between optical and THz pulses, the Cherenkov angle is large ( $\sim 64^\circ$  in  $\text{LiNbO}_3$  and  $\sim 69^\circ$  in  $\text{LiTaO}_3$ ), and hence polariton waves propagate primarily in lateral directions.

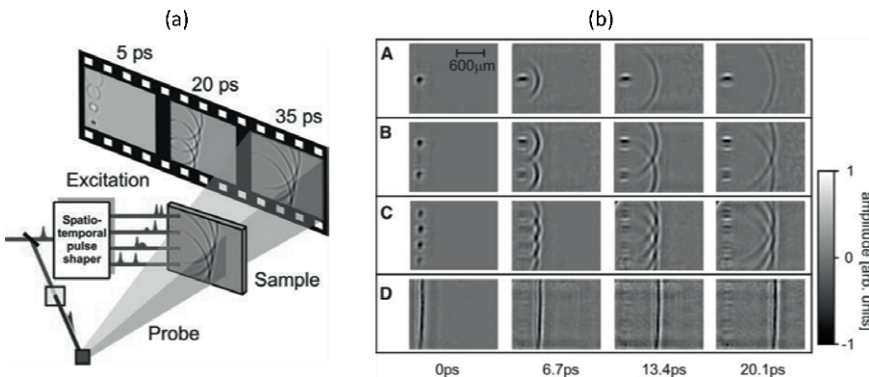


**Fig. 5.51.** (a) Schematic illustration of the spatiotemporal coherent control experiment. (b) Snap shots of polariton wave propagation in a  $\text{LiTaO}_3$  after impulsive excitation with (A) one, (B) two, (C) four, and (D) nine excitation regions. (From [174]. Reprinted with permission from AAAS.)

Figure 5.51(a) illustrates an experimental scheme to directly visualize the evolution of polariton waves excited by femtosecond optical pulses. The experimental setup exploits a time-resolved pump-probe technique. Going through an optical pulse shaper, a pump pulse is transformed into a spatially and temporally controlled multiple pulses. The shaped optical pulses generate polariton waves in a thin  $\text{LiNbO}_3$  or  $\text{LiTaO}_3$  crystal, which replicates the spatial and temporal profile of the pump pulses. Usually, polariton wave frequencies ( $\sim 1$  THz) are far below the lowest phonon resonance (extraordinary  $\omega_T/2\pi = 7.4$  THz for  $\text{LiNbO}_3$  and 6.0 THz for  $\text{LiTaO}_3$ ), thus the polariton waves propagate at a photon-like speed of  $\sim c/\sqrt{\epsilon(0)}$ . A spatially expanded

probe beam transmits through the crystal and maps out the index change induced by the polariton waves. Temporal evolution of polariton waves can be recorded as controlling the relative time delay between pump and probe pulses.

Figure 5.51(b) shows sequences of snap shots depicting propagation of polariton waves in a LiTaO<sub>3</sub> crystal after optical pulses simultaneously illuminate one, two, four, and nine spots lined up with the crystal optic axis. The coherent polariton wavepackets emerging from the excitation spots undergo constructive and destructive interferences and form a superposed wavepacket in the far field.

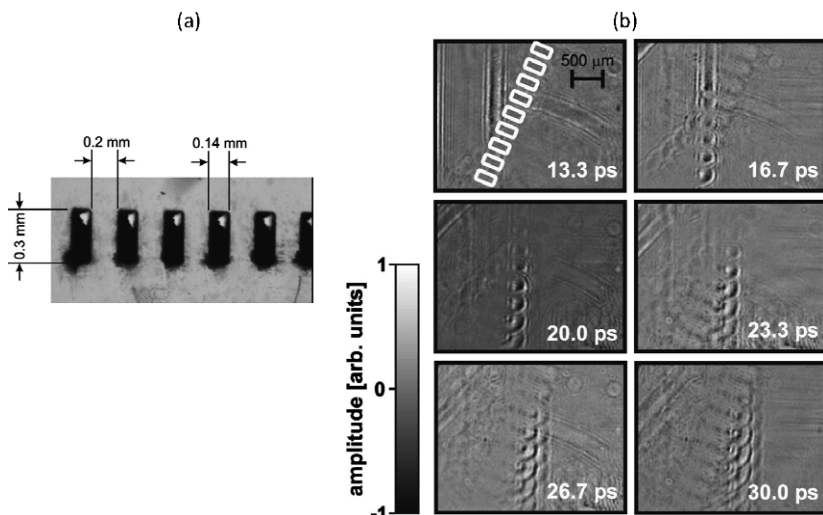


**Fig. 5.52.** (a) Optical micrograph of the laser-machined grating structure. (b) Evolution of a single-cycle polariton plane wave diffracted by the grating structure. (Reprinted with permission from [175]. ©2003, American Institute of Physics.)

In addition to the use of optical pulse shaping, permanent features patterned in a sample can manipulate polariton waves. A variety of polaritonic devices such as waveguides, resonators, and gratings have been demonstrated so far. Figure 5.52 shows an example that a polariton wave is diffracted by an integrated grating structure in a LiNbO<sub>3</sub> crystal. The grating pattern shown in Fig. 5.52(a) was imprinted in the sample by femtosecond laser machining. Figure 5.52(b) shows a sequence of snap shots illustrating that a single-cycle polariton plane wave is incident on the grating structure at an angle of 24°, passing through the structure while undergoing interferences and diffractions, and, eventually, building up the first- and second-order diffraction wavefronts.